Practical Implementation and Real-World Validation of Reconfigurable Intelligent Surfaces

by

Sefa KAYRAKLIK

A Dissertation Submitted to the
Graduate School of Sciences and Engineering
in Partial Fulfillment of the Requirements for
the Degree of

Master of Science

in

Electrical and Electronics Engineering

KOÇ ÜNİVERSİTESİ

July 25, 2023

Practical Implementation and Real-World Validation of Reconfigurable Intelligent Surfaces

Koç University

Graduate School of Sciences and Engineering

This is to certify that I have examined this copy of a master's thesis by

Sefa KAYRAKLIK

and have found that it is complete and satisfactory in all respects,

and that any and all revisions required by the final

examining committee have been made.

Committee Members:

____

Assoc. Prof. Ertuğrul BAŞAR (Advisor)

____

Prof. Sinem ÇÖLERİ

____

Prof. Ali Emre PUSANE

Date: ______________________

To my dear family,

ABSTRACT

Practical Implementation and Real-World Validation of Reconfigurable Intelligent Surfaces
Sefa KAYRAKLIK
Master of Science in Electrical and Electronics Engineering
July 25, 2023

Reconfigurable intelligent surface (RIS)-empowered communications represent exciting prospects as one of the promising technologies capable of meeting the requirements of the sixth generation networks, such as low latency, reliability, and dense connectivity. The literature still lacks real-world experimental applications implementing scenarios that suggest applicability. However, validation of test cases and real-world experiments of RISs are imperative to their practical viability. To this end, this thesis presents the implementation and experimentation of the RIS in order to reveal the RIS's potential for future-generation networks in the possible use cases of RIS-assisted wireless communication networks, such as coverage enhancement, physical layer security, spectrum sensing, and wireless data link management.

In Chapter 3, a physical demonstration of an RIS-assisted communication system is provided in an indoor environment in order to enhance coverage by increasing the received signal power. The performance of the RIS-assisted system is initially analyzed for a set of different locations of the receiver and observed around 10 dB improvement in the received signal power by careful RIS phase adjustments. Then, an efficient codebook design for RIS configurations is employed to adjust the RIS states on the move without feedback channels. The impact of an efficient grouping of RIS elements is investigated with the objective of reducing the training time needed to find the optimal RIS configuration. In the extensive experimental measurements, training time is reduced with the proposed grouping scheme from one-half to one-eighth by sacrificing only a few dBs in received signal power.

In Chapter 4, the performance of the RIS is characterized according to the practical measurements to implement physical layer security (PLS), on which the transmitter (Alice), the intended user (Bob), and the eavesdropper (Eve) are located in an indoor environment. The measurement-based validation of the RIS deployment

where the RIS is situated to maximize the secrecy capacity of the wireless communication system is still an insufficient stage although the theoretical framework of the PLS boosted by the RIS has been revealed in the literature. As of this point, it remains a challenge and an open question how the RIS can provide secure wireless communication in a practical measurement scenario by adjusting the RIS's phase shifts in such a way that the difference between the received signal power of Bob and Eve is increased to maximize the level of secrecy. The measurement campaign of the proposed system model of the RIS-aided PLS scheme demonstrates that the secrecy capacity can be significantly improved by introducing the RIS into the system with the assumption of the availability of Eve's power measurements.

In Chapter 5, an experimental demonstration of an RIS-empowered spectrum sensing system is presented, in which the object detection approach by deep-learning (DL) methods is utilized to detect the signal's type and location in the frequency and time domain. The state-of-art DL-based detectors of Detectron2 and YOLOv7 are trained with the spectrograms of the synthesized signal dataset of 4G LTE and 5G NR, in which the signals are treated as objects on an image. Introducing the RIS into the proposed measurement setup significantly improves the performance of the detectors due to the direct correlation between the received signal power and the performance of the spectrum sensing process.

In Chapter 6, the performance of a millimeter wave (mmWave) RIS prototype is validated with a vector network analyzer in an anechoic chamber as well as the evaluation of the considered RIS is performed with the fifth-generation (5G) waveform operating at the mmWave frequency band in a data center. In fact, link management in a data center is one of the possible playgrounds of RIS employment since rack cabinets cause severe blockage for the wireless communication system in the room. The measurements in the data center demonstrate that deploying the mmWave RIS into the data center provides improvements in received signal power.

ÖZETÇE

Yeniden Yapılandırılabilir Akıllı Yüzeylerin Pratik Uygulaması ve Gerçek Dünya Doğrulaması
Sefa KAYRAKLIK
Elektrik ve Elektronik Mühendisliği, Yüksek Lisans
25 Temmuz 2023

Yeniden yapılandırılabilir akıllı yüzey (RIS) destekli haberleşme sistemleri, düşük gecikme süresi, güvenilirlik ve yoğun bağlantı gibi altıncı nesil ağların gereksinimlerini karşılayabilecek gelecek vaat eden teknolojilerden biri olarak heyecan verici beklentiler sunmaktadır. Literatür, uygulanabilirliği gösteren senaryoları hayata geçiren deneysel uygulamalardan hâlâ yoksundur. Bununla birlikte, test senaryolarının doğrulanmasını ve RIS'lerin gerçek dünya deneylerini gözlemlemek, RIS'in pratikte uygulanabilirliğini göstermek için zorunludur. Bu amaçla, bu tez, kapsama alanını genişletme, fiziksel katman güvenliği, spektrum algılama ve kablosuz veri bağlantısı yönetimi gibi RIS destekli kablosuz iletişim ağlarının olası kullanım durumlarında RIS'in gelecek nesil ağlar için potansiyelini ortaya çıkarmak amacıyla RIS'in uygulanmasını ve deneylerini sunmaktadır.

Bölüm 3'te, alınan sinyal gücünü artırarak kapsama alanını genişletmek için kapalı ortamda RIS destekli bir haberleşme sisteminin fiziksel gösterimi sağlanmıştır. RIS destekli sistemin performansı, başlangıçta alıcının bir dizi farklı konumu için analiz edilmiş ve özenli RIS faz ayarlamaları ile alınan sinyal gücünde yaklaşık 10 dB iyileşme gözlemlenmiştir. Ardından, RIS konfigürasyonları için kod çizelge tasarımı, alıcı hareket halindeyken geri besleme kanalları olmadan RIS'in yansıtıcı elemanlarının durumlarını ayarlamak için kullanılmaktadır. Optimum RIS konfigürasyonunu bulmak için gereken işlem süresini azaltmak amacıyla RIS elemanlarının verimli bir şekilde gruplandırılmasının etkisi incelenmiştir. Kapsamlı deneysel ölçümlerde, önerilen gruplama şeması ile işlem süresi, alınan sinyal gücünde yalnızca birkaç dB feda edilerek yarı yarıyadan sekizde bire kadar düşürülmüştür.

Bölüm 4'te, fiziksel katman güvenliğinin (PLS) sağlanması için RIS'in karakterizasyonu, verici (Alice), asıl alıcı (Bob) ve gizli dinleyicinin (Eve) kapalı ortama yerleştirildiği pratik ölçümlere dayanarak gösterilmiştir. RIS ile güçlendirilmiş

PLS'nin teorik çerçevesi literatürde ortaya konmuştur ancak kablosuz haberleşme sistemlerinin gizlilik kapasitesini en üst düzeye çıkarmak için RIS'in kullanımı önerilen ölçüm tabanlı doğrulaması hâlâ yetersiz bir aşamadır. Gelinen noktada, RIS elemanlarının faz kaymalarını ayarlayarak pratik bir ölçüm senaryosunda RIS'in güvenli kablosuz iletişim sağlama yeteneğini doğrulamak zorlu ve açık bir soru olmaya devam etmektedir. Ölçümlerde Bob ve Eve'nin alınan sinyal güçleri arasındaki farkı artıracak şekilde RIS faz kaymalarını ayarlanmış ve böylece gizlilik kapasitesi en üst düzeye çıkarılmıştır. Eve'in güç ölçümlerinin ulaşılabildiği varsayımıyla RIS destekli PLS senaryosunun ölçümü, RIS'in sisteme dahil edilmesiyle gizlilik kapasitesinin önemli ölçüde iyileştirilebileceği gösterilmiştir.

Bölüm 5'te, sinyalin frekans ve zaman alanındaki konumunu ve sınıfı tespit etmek için derin öğrenme (DL) yöntemleriyle nesne algılama yaklaşımının kullanıldığı, RIS ile güçlendirilmiş spektrum algılama sisteminin deneysel bir gösterimi sunulmuştur. Son teknoloji ürünü DL tabanlı Detectron2 ve YOLOv7 dedektörleri, 4G LTE ve 5G NR sinyallerinin bir görüntü üzerindeki nesneler olarak ele alındığı sentezlenmiş sinyal veri setinin spektrogramlarıyla eğitilmiştir. Alınan sinyal gücü ile spektrum algılama sürecinin performansı arasında doğrudan bir korelasyon bulunmaktadır. Bu yüzden, RIS'in önerilen ölçüm düzeneğine dahil edilmesi spektrum algılama yöntemlerinin performansını önemli ölçüde artırmıştır.

Bölüm 6'da, milimetre dalga (mmWave) RIS prototipinin performansı, yankısız bir odada bir vektör ağ analizörü ile doğrulanmış ve ele alınan RIS'in performans değerlendirilmesi, veri merkezinde mmWave frekans bandında çalışan beşinci nesil (5G) dalga formu ile gerçekleştirilmiştir. Aslında bir veri merkezindeki bağlantı yönetimi, RIS kullanımının olası uygulama alanlarından biridir çünkü server raf kabinleri, veri merkezi odasındaki kablosuz haberleşme sistemi için ciddi blokaja neden olmaktadır. Veri merkezindeki ölçümler, mmWave RIS'in veri merkezine yerleştirilmesinin alınan sinyal gücünde iyileştirmeler sağladığını göstermiştir.

ACKNOWLEDGMENTS

I would like to express my heartfelt appreciation to my advisor Assoc. Prof. Ertuğrul Başar for his guidance, support, and motivation during the course of my research. I cannot overstate the immense value that his expertise and insightful perspectives brought to bear in the process of shaping my ideas and refining my work. I consider myself incredibly fortunate to have been granted the privilege of collaborating with him. Also, I am grateful for the opportunity to be part of his exceptional team, CoreLab. I would like to thank my friends and labmates for their support and motivation.

I would like to express my utmost gratitude to my parents for the love, support, and encouragement that they have bestowed upon me throughout my life. No matter what, they guided me in distinguishing between right and wrong and consistently placed their trust in my ability to find the correct path. The sacrifices and guidance will forever be in my heart.

I wish to extend my sincere gratitude to my esteemed colleagues and friends at TÜBİTAK BİLGEM HİSAR Lab. for their guidance, support, and advice during my research. Having their encouragement, constructive feedback, and companionship made this journey more fulfilling and enjoyable for me. I consider myself privileged to have been granted the opportunity to collaborate with such skilled and devoted individuals, and I eagerly anticipate the prospect of furthering our collaboration in the future.

TABLE OF CONTENTS

LIST OF TABLES

LIST OF FIGURES

ABBREVIATIONS

AP	Average Precision
COCO	Common Objects in Context
CR	Cognitive Radio
CSI	Channel State Information
dBFS	decibels Relative-to-Full-Scale
DL	Deep Learning
EMF	Electromagnetic Field
ETSI	European Telecommunications Standards Institute
FAIR	Facebook AI Research
IM	Index Modulation
ISG	Industry Specification Group
LoS	Line-of-Sight
mAP	mean Average Precision
MIMO	Multiple Input Multiple Output
mmWave	Millimeter Wave
PHY	Physical
PLS	Physical Layer Security
PR	Primary Receiver
PT	Primary Transmitter
PU	Primary User
RF	Radio-Frequency
RIS	Reconfigurable Intelligent Surface
THz	Terahertz
SDR	Software-Defined Radio
SINR	Signal-to-Interference-plus-Noise

SNR	Signal-to-Noise
SSB	Synchronization Signal Block
SU	Secondary User
Rx	Receiver
Tx	Transmitter
UPA	Uniform Planar Array
VNA	Vector Network Analyzer
YOLO	You Only Look Once
3GPP	3rd Generation Partnership Project
4G LTE	Fourth Generation Long-Term Evolution
5G	Fifth Generation
5G NR	Fifth Generation New Radio
6G	Sixth Generation

Chapter 1

INTRODUCTION

The fifth generation (5G) wireless communication technology has been actively deployed worldwide since its definition at the 3rd Generation Partnership Project (3GPP) Release 15 [1]. Though 5G technology is designated to offer upgraded mobile broadband and ultra-reliable low-latency communications, it is still uncertain whether it can accommodate upcoming Internet-of-Everything applications [2]. In order to address this issue, both academy and industry have been extensively studying cutting-edge technologies and creating innovative concepts for the sixth generation (6G) wireless communication networks. Nevertheless, the demanding and compelling features that come with these innovative and exciting applications include ultra-reliability, low-latency, extremely high data rates, spectrum optimization, and dense connectivity. In order to meet these demanding requirements of 6G, sophisticated physical (PHY) layer approaches have been put forward. Utilizing efficient PHY layer techniques such as ultra massive multiple-input multiple-output (MIMO) systems, index modulation (IM), terahertz (THz) frequency bands (over 100 GHz), and reconfigurable intelligent surfaces (RISs) could be the way out to enable the appealing characteristics of 6G. RISs are composed of passive reflecting elements, which can be software adjusted to effectively direct the reflected signals toward any desired location collaboratively. Recently, researchers are becoming more and more interested in RIS-aided communication due to its clear promise for improving link capacity, minimizing interference, strengthening secure communication, and extending the coverage [3, 4, 5]. RIS-aided communication has begun to be considered a strong candidate to become a possible component of 6G systems alongside other strong candidates such as ultra-massive MIMO and THz communication [6, 7].

As a consequence of the above-mentioned expected benefits, it is evident that RIS-aided schemes gleam as an attractive pathway for future wireless communications. In order to address certain requirements of 6G, researchers have recently studied various attractive RIS-empowered solutions. Yet, to demonstrate the practical feasibility of an advancing technology such RISs in ongoing next-generation network operations, test case validations, field tests, and real-life experiments are crucial. Therefore, implementation and experimentation of the RIS into the possible use cases of RIS-assisted wireless communication networks, such as coverage enhancement, physical layer security, spectrum sensing, and wireless data link management, are necessary to reveal the RIS's potential for future-generation networks.

1.1 Related Works

In spite of the fact that most RIS studies concentrate on theoretical perspectives, practical measurements-based research that demonstrates the benefits of RIS-aided wireless communication systems in real-world conditions is recently gaining popularity [8, 9, 10, 11, 12, 13, 14, 15, 16, 17]. In this context, a set of experimental research based on developed testbeds has been conducted, and realistic transmission scenarios of the RISs have been investigated. The authors of [8] realized a model for the path loss of a RIS-aided wireless communication channel in a blocked line-of-sight (LoS) link between the transmitter and receiver. Their results demonstrated that the proposed models are able to estimate the measurements. In [9], the authors proposed an algorithm for optimizing the RIS configuration by utilizing the RIS's geometrical array structure and the received signal power of the receiver. The measurements in both indoor and outdoor environments are completed with an RIS prototype of 1100 reflecting elements, and the results are the improvement of 26 dB power gain in the indoor environment and 27 dB and 17 dB power increase for 50 m and 500 m distances in the outdoor environment, respectively. In [10], a received signal power model of an RIS-empowered wireless communication network is proposed by exploring a radar cross-section-based method in order to verify the proposed model via the measurements of the received power. The authors in [11] initially proposed a custom-developed continuous phase-shifted RIS operation in an indoor environment. Continuous phase surfaces serve more degrees of freedom than discrete phase shift RISs in terms of manipulating radio patterns owing to a more prosperous number of tunable phases. By employing this continuous phase surface, this study utilized software-defined radio (SDR) broadcasting video signals at the carrier frequency of 3.5 GHz. The researchers also investigated the received power performance for different receiver locations located at different angles with respect to the RIS in an L-shaped indoor environment [11]. Furthermore, an RIS is also deployed in another similar L-shaped indoor test scenario for coverage enhancement purposes, where only a non-line-of-sight channel is available [12]. This system deploys an RIS with several columns of sub-wavelength unit cells where each has a 3-bits phase resolution due to their custom hardware. This work also examined the received power performance of users positioned at various positions with monopole and horn antennas. Furthermore, the performance of binary unit cells to control millimeter wave (mmWave) beamforming in both near-field and far-field conditions is investigated in [13]. 1-bit RIS as a passive access point extender is proposed for mmWave communications in [14]. Four-state reflection in sub 6GHz frequencies is studied in [15]. Moreover, instead of discrete phase shift designed schemes, [16] implemented a continuous phase reflecting scheme driven by a varactor-controlled surface. Finally, [17] investigated omni-scope transmission exploiting the joint progress of reflective and refractive features of RIS.

It is worth noting that none of the measurement-based studies discussed above didn't utilize the RIS in the scenarios for the implementation of the physical layer security (PLS), on which several theoretical schemes have been provided in [18, 19, 20, 21]. In [18], the authors analytically derived the secrecy outage probability for the case of the legitimate user and the eavesdropper receiving the transmitted signals from both the direct channel of the transmitter and through the reflected signals of the RIS. The proposed analytical model estimates the improvement in the secrecy outage probability in terms of the number of the RIS's reflecting elements. The authors of [19] maximized the secrecy capacity by cooperatively utilizing the capability of the base station's active beamforming and the capability of the RIS's passive beamforming. In [20], the authors presented the characterization of the RIS-aided downlink transmission in the PLS scenario for randomly positioned users and a multi-antenna eavesdropper, exploiting the stochastic geometry theory. In fact, they composed the derivation of the exact probability distribution of the received signal-to-interference-plus-noise (SINR) ratio and provided the analytical performance metrics for security. The authors of [21] proposed an RIS-empowered MIMO system for an PLS scenario with the assumption of perfectly knowing the legitimate user's channel state information (CSI) at the transmitter, yet the CSI of the eavesdropper being absent the transmitter. The optimization of the covariance matrix of the transmitter and the adjustment of the phase shifts of the RIS's reflecting elements were iteratively acquired to minimize the transmit power in order to employ the remaining transmit power to convey the artificial noise for the interception of the eavesdropper.

None of the measurement-based works mentioned at the beginning of the section consider the RIS in the spectrum sensing system, yet a theoretical background of the RIS-enhance spectrum sensing systems has been introduced by several studies [22, 23, 24, 25, 26, 27]. In [22], the authors derived the performance metrics of the transmission probability of the secondary user (SU), the system's throughput, and the probabilities of false alarm and detection in an RIS-assisted cognitive radio (CR) network. Their results demonstrated the improvement in the spectrum sensing task achieved by introducing the primary user (PU)-controlled RIS into the CR network. The authors of [23] presented an RIS-enhanced energy detection framework for the spectrum sensing task. They derived the closed-form expressions of the average detection probabilities for the cases of presence and absence of the direct link and validated their theoretical analysis through simulations. The authors of [24] presented a weighted energy detection approach for the RIS-aided spectrum sensing system in the CR networks where the capability of passive beamforming and the large aperture of the RIS are utilized to improve the received signal power of SU from the PU. In [25], the authors derived the detection probabilities for two cases in which the RIS supports the reception of the SU and the reception of the PU's receiver. Their results showed that the RIS provides substantial improvement in the spectrum sensing task for both cases of deployment. The authors of [26] implemented the maximum eigenvalue detection method to an RIS-empowered spectrum sensing system in which the RIS serves to decrease the signal samples required to achieve the desired detection probability. They derived the theoretical estimation for the number of the RIS's reflecting elements to accomplish close to 1 detection probability and verified their derivations through simulations. In [27], the authors proposed a new detection threshold regarding the false alarm rate to improve the performance of the spectrum sensing task in the RIS-assisted CR network where the RIS is optimized with two stages of sensing and transmission.

1.2 Contribution of The Thesis

Against this background, the literature is still premature for real-world experimental applications accommodating use-case scenarios of RISs implying applicability. The main contributions of the thesis are summarized as follows.

- Given that the first step toward RIS-assisted systems is passive beamforming techniques, the behavior of the RIS is realistically analyzed with respect to the receiver allocation points, a new line of practical applications by incorporating a codebook design into RIS is introduced without going through the optimization of RIS configurations, and an efficient grouping scheme for the RIS elements is proposed in order to reduce the training time spent in the process of deciding the optimal RIS configurations.

- As utilizing the RIS in the task of physical layer security, the mathematical expression of the secrecy capacity is derived in the RIS-aided wireless communication system in terms of the received signal powers of Bob and Eve, and the RIS's capability of handling the PLS problem by increasing the secrecy capacity of the system is demonstrated via a measurement-based characterization.

- In deploying the RIS into the spectrum sensing system, two state-of-art object detectors are trained in order to utilize and compare their performance in the spectrum sensing problem, and the improvement of introducing the RIS into the spectrum sensing system is exhibited by illustrating the performance increases of the detectors.

- In exploring the performance of a mmWave RIS prototype, the mmWave RIS's performance is verified in a perfect environment like an anechoic chamber, and the signal power improvement of 5G waveform running in the mmWave frequency band is examined by deploying the RIS into the wireless communication network in a data center.

1.3 Organization of The Thesis

The organization of the thesis is as follows: In Chapter 2, the general background knowledge about RISs is given, and also the possible use cases of the RIS are provided. Chapter 3 provides the measurements of the RIS-assisted communication for the purpose of enhancing the signal coverage through the reflected signals from the RIS. Chapter 4 discusses the secrecy capacity in the RIS-assisted PLS system and presents the characterization of the RIS's behavior in the PLS scenario via measurements. In Chapter 5, the RIS is utilized in a spectrum sensing system to boost the performance of the detectors utilized in the secondary user and validation of the improvement, which is obtained by introducing the RIS into the spectrum sensing process is provided through measurement. Chapter 6 validates the performance of the mmWave RIS prototype in an anechoic chamber and demonstrates the resulting enhancement of deploying the RIS into a data center via 5G mmWave signals. At last, Chapter 7 concludes the thesis.

Chapter 2

RECONFIGURABLE INTELLIGENT SURFACES FOR FUTURE WIRELESS NETWORKS

In this chapter, the general background knowledge about reconfigurable intelligent surfaces (RISs) is provided with a brief overview. Additionally, the possible use cases of the RISs for the future generation of wireless communication networks are summarized according to the reports of standards groups.

2.1 RIS Overview

RISs have been identified as a promising candidate technology for future-generation networks that has the capability of intelligently manipulating the wireless signal propagation channel. The structure of the RIS incorporates a surface of a planar array reflecting antennas, whose physical properties can be individually adjusted in order to control their amplitude and phase responses subject to the incoming signal. With the RIS's capability of exploiting the signal propagation environment via the magnitude and phase adjustments of the reflecting elements, RIS provides a variety of practical benefits in the implementation of wireless communication networks. The RIS doesn't require advanced signal processing hardware like radio-frequency (RF) chains since its reflecting elements comprise cheap microstrip being controlled with diodes. In fact, the RIS presents an energy and cost-efficient solution with a lightweight, low profile, and suitable geometry node to the wireless communication system. Additionally, the RIS suggests a feasible implementation scenario with massive deployment in the wireless network in order to boost the spectral efficiency of the network.

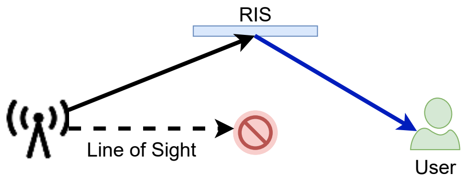

Figure 2.1: Constituting virtual LOS through the RIS in the case of blockage.

2.2 Use Cases

RIS brings about new enabling wireless communication technologies with the help of dynamically controlling the propagation channel of the radio signals to accomplish certain objectives. There have been some initiations about describing these objectives in specific use cases by standards organizations such as 3rd Generation Partnership Project (3GPP) and European Telecommunications Standards Institute (ETSI). ETSI has established an Industry Specification Group (ISG)[1] to address RIS pre-standardization studies by identifying the technology and filling the standards gaps for the arising RIS technology. The first group report of the ETSI ISG RIS [28], which includes use cases, deployment scenarios, and requirements for the RIS technology, has been publicly shared. In the group report, the ISG RIS has been agreed on defining eight key use cases for the RIS applications: coverage enhancement, spectral efficiency, beam management, physical layer security, localization accuracy, sensing capacity, energy efficiency, and link management [28].

The first use case of the RIS is signal coverage enhancement which describes a solution for the common problem of wireless communication networks, which is the uneven signal coverage and blockage of the line-of-sight (LoS) link due to the obstacles like trees, buildings, and walls. In these poor coverage regions, users may unable to receive the promised quality of service. Adding extra access points to cover these areas is an expensive and inefficient solution. Therefore, the RIS is a promising candidate with easy and economical implementation to solve the uneven coverage problem raised by the blockage. Figure 2.1 illustrates a simple implementation of

[1]Further information is available at: https://www.etsi.org/technologies/reconfigurable-intelligent-surfaces

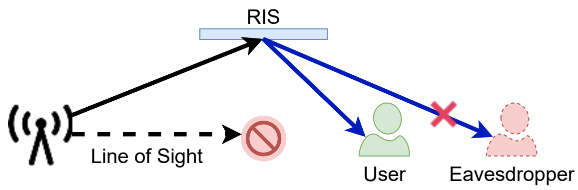

Figure 2.2: Establishing secure wireless communication via the RIS.

the RIS, where the virtual LoS is formed through the RIS in the case of blocked LoS.

The second application is the spectral efficiency on which the wireless channel between the transmitter and receiver has a strong correlation limiting the multiple data transmission. The deployment of the RIS can diminish this problem by introducing additional reflection paths, resulting in more eigen channels, which increase spectral efficiency and spatial multiplexing gains. In fact, enhancing the signal coverage by improving the received signal power through the RIS also increases spectral efficiency.

The third use case is beam management, whose objective is to alleviate the losses of signal propagation over wireless transmission by constructing and preserving the beam pair links between the transmitter and receiver, resulting in the improvement of spectral efficiency and stable signal coverage, specifically for the high frequencies. The beamforming capability of the RIS facilitates focusing the signal beams toward certain users or directions. In fact, the alternative beams from the RIS can be dynamically adjusted according to the channel conditions in an energy and cost effective way.

The fourth usage of the RIS is physical layer security, on which the eavesdroppers can reach confidential signals due to uncontrolled wireless propagation channels. Establishing an adjustable and smart propagation environment through utilizing RIS is an efficient way of preventing confidential signals from being leaked to eavesdroppers and enhancing the security of wireless communication channels. Figure 2.2 demonstrates an example diagram of a secure communication where the RIS diminishes signals reaching the eavesdropper while boosting the user's received signal power.

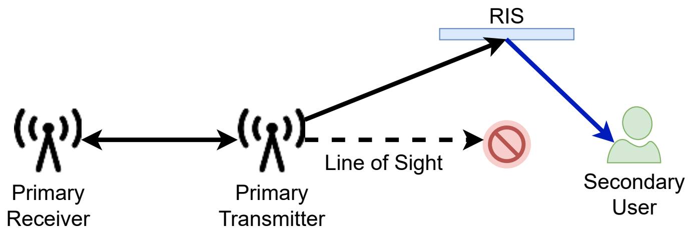

Figure 2.3: Boosting spectrum sensing performance utilizing RIS.

The fifth application of the RIS is localization accuracy which is restricted by the number of base stations in the network and the presence of an LoS link. Introducing RIS into the communication system is cheaper and more adaptable in comparison with the deployment of a new base station. Wireless communication systems can increase their position accuracy and spatial resolution with the help of the RIS.

The sixth usage of the RIS is sensing capabilities on which many emerging technologies coming with the new generation wireless networks (i.e., future fifth generation and sixth generation) demand both communication and sensing functionalities. The sensing procedure mostly relies on the LoS connection between the transmitter and receiver, whereas performing the sensing process with non-LoS links is quite a challenging task. Therefore, introducing the RIS into the sensing system enhances the sensing performance by constructing a virtual LoS link to sense the environment. One of the sensing implementations is spectrum monitoring in order to utilize the spectrum more efficiently in the scenario of the primary and secondary user. Figure 2.3 shows an example system model for an RIS-enhanced spectrum sensing system where the secondary user monitors the activities of the primary transmitter and operates when the primary transmitter is idle.

The seventh application of the RIS is energy efficiency, whose applications are wireless power transfer, energy harvesting, power saving, and electromagnetic field (EMF) exposure minimization. The RIS can provide a virtual LoS link between the transmitter and receiver in the tasks of power transfer and energy harvesting. In addition, deploying the RIS as a new node in the wireless communication networks for both indoor and outdoor environments will assist in diminishing the networks'

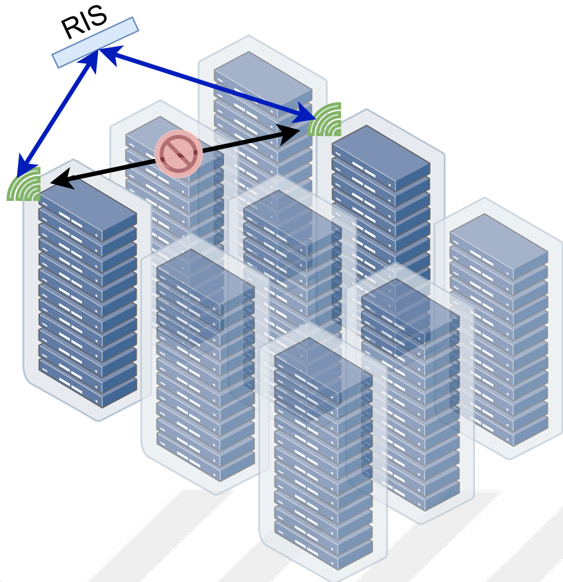

Figure 2.4: Managing wireless data links via the RIS in a data center.

power consumption, resulting in power saving in the networks. Moreover, introducing the RIS into wireless communication systems can contribute the signal coverage without substantially intensifying the systems' transmission power since the RIS exploits currently available signals in the propagation environment.

The eighth use case of the RIS is link management in data centers which deploys wireless data transmission between the servers to reduce the connection complexity and cabling costs. Deploying the RIS into the wireless signal channel, which can be fixed to the ceiling or rear panel of the server racks, gives the opportunity to remotely and dynamically adjust the wireless link between the servers. Figure 2.4 illustrates an example deployment of the RIS into a data center, which helps wireless data transmission.

Chapter 3

RIS-ASSISTED COVERAGE ENHANCEMENT

In this chapter, a physical demonstration of an RIS-assisted communication system is presented in an indoor environment in order to enhance the coverage by increasing the received signal power. The literature still lacks real-world experimental applications implementing scenarios that suggest applicability. Proposed systems in the literature reveal some challenges that restrict their viability in practical use cases due to their computational burden and complexity. At this point, improving and optimizing RIS control processes become critical to obtain the optimal gains that the existing RIS technologies can provide.

Given that the first step toward RIS-assisted systems is passive beamforming techniques, the three targets of this chapter are (i) to realistically analyze the behavior of the RIS with respect to the receiver allocation points, (ii) to present a new line of practical applications by incorporating a codebook design into RIS without going through the optimization of RIS configurations, and (iii) to employ an efficient grouping scheme for the RIS elements in order to reduce the training time spent in the process of deciding the optimal RIS configurations.

3.1 System and Signal Model

As illustrated in Figure 3.1, a basic wireless communication system where the RIS assists the signal transmission between a single-antenna transmitter (Tx) and receiver (Rx) is considered. The RIS utilized in the system model has a form of a uniform planar array (UPA) with $N = N_x \times N_y$ elements with binary phase shifts of $0°$ and $180°$. The channels from the Tx and Rx to the RIS are defined as $\mathbf{h} \in \mathbb{C}^N$ and $\mathbf{g} \in \mathbb{C}^N$, respectively. The direct line-of-sight (LoS) channel between the Tx and Rx is described as $h_{LoS} \in \mathbb{C}$. Accordingly, with $x[k]$ being the complex baseband

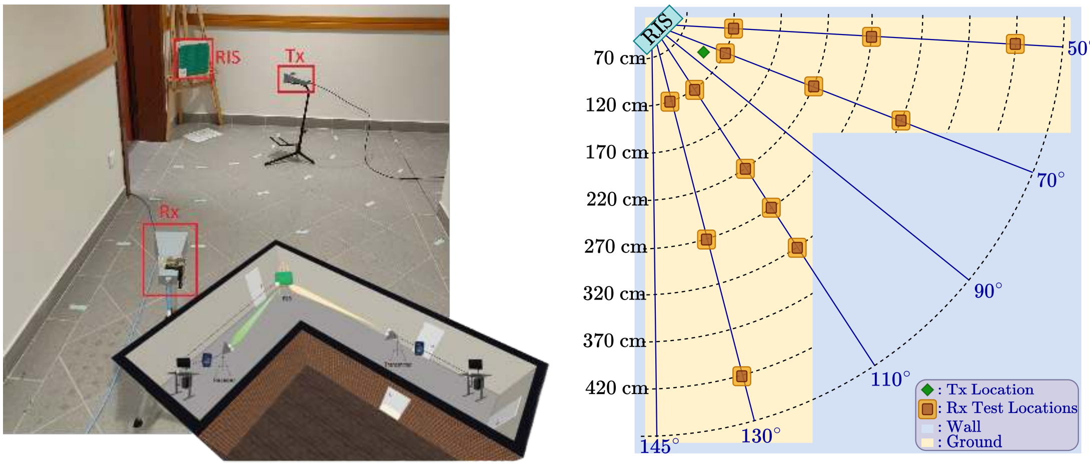

(a) (b)

Figure 3.1: (a) The considered measurement setup of the RIS-aided wireless communication system in an indoor office environment, and (b) the top view of the setup with all Rx test locations.

transmitted signal, the received signal $r[k]$ can be written as

$$r[k] = \left(\mathbf{g}^H \boldsymbol{\Theta} \mathbf{h} + h_{LoS}\right) x[k] + n[k], \tag{3.1}$$

where $n[k] \sim \mathcal{N}_{\mathbb{C}}\left(0, \sigma_n^2\right)$ represents the noise component at the receiver, and $\boldsymbol{\Theta}$ represents the RIS configuration matrix, defined as diag$\left\{\alpha_1 e^{j\phi_1}, \cdots, \alpha_N e^{j\phi_N}\right\}$, whose diagonal entries denote the states of the RIS elements. Since in the considered prototype, the RIS elements are passive and binary-phased, α_n is constant and ϕ_n takes values of only 0° and 180°. Furthermore, the LoS component of the received signal is neglected since, as seen in Figure 3.1, horn antennas, whose half beamwidth is 40°, are used in the Tx and Rx to transmit and receive signals, and the direct link between the terminals are out of the beamwidth of the antennas.

One of the primary purposes of using an RIS in the transmission is to increase the signal-to-noise ratio (SNR) at the Rx by enabling anomalous reflections from the RIS, thereby enhancing the signal coverage. The SNR is proportional to end-to-end gain $\left|\mathbf{g}^H \boldsymbol{\Theta} \mathbf{h}\right|^2$, neglecting the LoS link between the terminals due to the non-intersecting antenna beams and can be adjusted by modifying the RIS configuration matrix $\boldsymbol{\Theta}$. Thus, the optimum configuration matrix of the RIS, $\boldsymbol{\Theta}^*$, which maximizes the end-to-end gain, is determined as the following expression:

$$\begin{aligned} \boldsymbol{\Theta}^* &= \arg\max_{\phi_n,\forall n} \left|\mathbf{g}^H \boldsymbol{\Theta} \mathbf{h}\right|^2 \\ &\qquad \text{s.t. } \phi_n \in \{0^\circ, 180^\circ\}, \quad \forall n. \end{aligned} \tag{3.2}$$

In the practical setup, based on the maximization problem given in (3.2), without going through the channel estimation procedure, the objective function is considered as the average received signal power. The received signal powers are measured, and the objective function is optimized with an iterative method to obtain the RIS configuration, which maximizes the received signal power and focuses the reflected beam toward the Rx.

3.2 Measurement Setup and Scenarios

The considered system architecture of the RIS-assisted measurement setup is illustrated in Figure 3.1. The measurement campaign is conducted in an L-shaped hallway of an indoor office environment with the help of two ADALM-PLUTO software-defined radio (SDR) modules for transmission and reception of over-the-air signals, $x[k]$. In the measurement setup, the RIS is mounted on the hallway's corner while the antennas of the Tx and Rx SDRs are positioned at various angles and distances from the center of the RIS throughout the measurement process.

The RIS prototype developed by Greenerwave [29] is used to focus the transmitted signal in the desired direction via software-controlled phase shifts. The working bandwidth of the RIS is 1 GHz around the center frequency of 5.2 GHz. The RIS has a UPA structure with a 10×8 element grid, yet the right corner of the 2×2 part is preserved for its controller, ending up with a total of 76 reflecting elements whose reflection coefficient can be adjusted with PIN diodes. The PIN diodes can configure the phase shifts of the reflecting elements as 0° or 180°. Furthermore, each element contains two PIN diodes corresponding to horizontal and vertical polarization, resulting in four possible states for each element.

Through the measurement process, the Tx SDR sends a single-tone sinusoidal signal of 100 kHz at the carrier frequency of 5.2 GHz toward the RIS using a horn antenna, and the reflected signal from the RIS reaches the Rx SDR to measure

Algorithm 1 Iterative Method

Input: P_r, N, and S

Output: *States*

initiate *States* of RIS elements with OFF
$P_{max} \leftarrow 0$
for $i = 1$ to N **do**
    for $j = 1$ to S **do**
        apply state j to ith element
        measure P_r
        if $(P_r > P_{max})$ **then**
            update ith element of *States* with state j
            $P_{max} \leftarrow P_r$
        end if
    end for
end for
return *States*

the received signal power at 5.2 GHz. The configuration for the RIS, which directs the reflected beam toward the Rx SDR, is determined by observing the received signal power. Since all possible RIS configurations of 4^{76} are not efficient to be applied through an exhaustive search algorithm, a straightforward iterative method [14] attempts to find the RIS configuration, which will allow incoming signals to be reflected at the desired angle. Initially, all elements are set to OFF, indicating that the RIS is in no-phase-shift mode. Then, the four possible states of the first element are applied, and the RIS is kept in the state, resulting in the maximized received signal power at the Rx SDR. After determining the state of the first element, the same procedure is individually repeated for each of the remaining elements. The summary of the iterative phase adjustment method is given in Algorithm 1, where the measured received power and the obtained maximum received power are denoted as P_r and P_{max}, respectively, and S represents the number of RIS states for one element.

Algorithm 1 determines *States* containing RIS configuration that maximizes the received signal power at the Rx SDR. The received signal power is calculated by using the time samples captured at the center frequency of 5.2 GHz and moved to the complex baseband by the Rx SDR. Since ADALM-PLUTO SDR has a 12-bit analog-to-digital converter, the sampled complex baseband signals can be represented as integers in the range of $(-2047, 2048]$. Therefore, the received signal power is computed in the decibels relative to full scale (dBFS) via the equation:

$$P_{dBFS} = 10 \log_{10} \left(\frac{1}{K} \sum\nolimits_{k}^{K} |r[k]|^2 \right), \tag{3.3}$$

where P_{dBFS} denotes the average power of the received complex baseband signal $r[k]$, and the total number of received samples is K.

In the considered setup illustrated in Figure 3.1, the objective is to enhance the signal coverage in an indoor environment by increasing the received signal power via the deployment of an RIS to the communication network. In the transmission and reception of the signals, horn antennas provide control over the direction of the signals, while the considered measurement environment involving an L-shaped hallway prevents the direct link between the Tx and Rx SDR.

The hallway is formed as a grid according to angles, defined clockwise from the RIS surface as $\{50°, 70°, 90°, 110°, 130°, 145°\}$, and distances from the RIS as $\{70, 120, 170, 220, 270, 320, 420\}$ cm. As shown in Figure 3.1b, the intersections of the lines of angles and distances denote the grid representation, which is used in the practical measurements. The Tx SDR is placed on a fixed point at 78°, and 100 cm directed to the RIS, and the Rx SDR's antenna, which is considered to belong to a mobile user, is moved between the grid points based on the measurement scenarios.

Three different experiment scenarios are investigated in the course of the measurement campaign, which aims to focus the reflected beam of the RIS toward the user: In the first trial, the Rx SDR is positioned at different angles and distances to observe the performance of the RIS for the considered test points. In the second experiment, a codebook is formed for pre-determined test points on the grids to eliminate the feedback channel from the Rx to the RIS, which is employed during the process of determining the RIS configuration on the move. Throughout the experiment, the Rx SDR's antenna is moved along the test points at the interior regions of the grids. The performance comparisons for the test points are conducted between the offline codewords from the saved codebooks and the RIS configurations of the online iterative method, which is obtained from Algorithm 1. Finally, in the last scenario, the effect of grouping the RIS elements for joint phase adjustment is evaluated by reducing the training time required for selecting the configuration of the RIS.

3.3 Measurement Results

In this section, the results from several experiments using the RIS prototype to test the performance of the RIS in real-world communication scenarios are presented. Moreover, an efficient grouping strategy for the RIS elements is investigated in the L-shaped indoor environment to decrease the high training overhead burden on the RIS controller.

Throughout the experiments, the RIS is controlled with a Python script, which takes a Boolean array of 152 elements corresponding to PIN diodes of the horizontal and vertical polarization states. In the Boolean array, 0 and 1 correspond to no-phase-shift and 180°-phase-shift mode, respectively. The sampling rate of the Tx and Rx SDR are set to 1 MHz. The buffer size of the Rx SDR, the number of time samples to calculate the received signal power to be used in Algorithm 1, is selected as 10000.

3.3.1 Performance Analysis for Various Angles and Distances

The improvement in the power of the received signal via the RIS at the Rx will largely depend on the distance between the terminals. On the other hand, the variations in the position of Rx will alter the angle-of-arrival of the incoming signal from the RIS as well as the RIS-Rx distance. In order to analyze the performance of the RIS-assisted transmission systems for varying angles, the Rx SDR's antenna is placed at 13 different test points on the grid, which are illustrated in Figure 3.1b as brown squares.

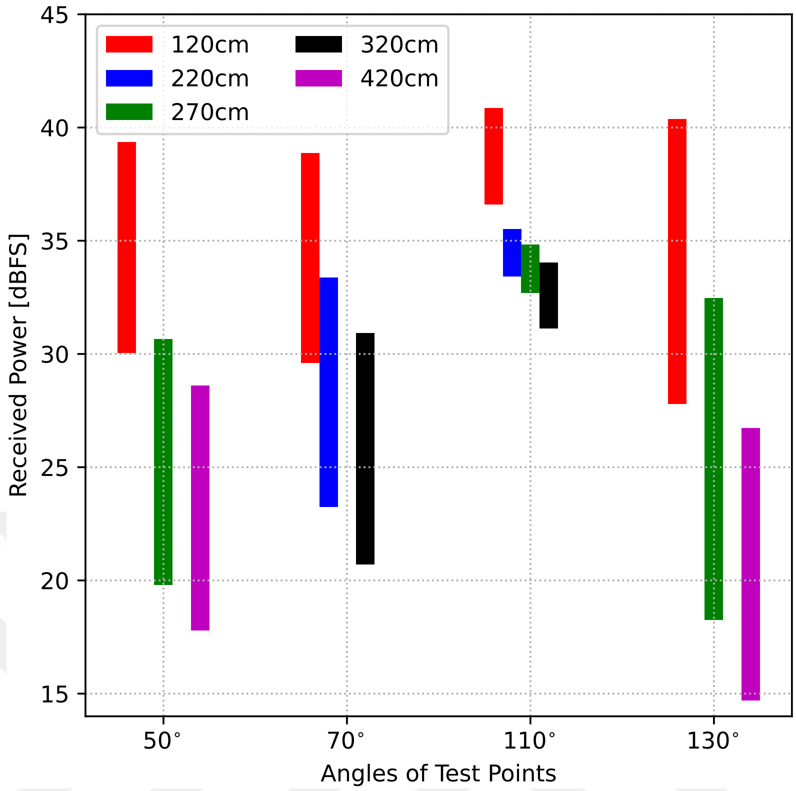

Figure 3.2: The received power comparison for various locations of the user.

Figure 3.2 shows the comparison of the received signal power for these test points when the RIS configuration obtained with Algorithm 1 is applied. For example, the green bar for the angle of 50° in Figure 3.2 illustrates that the received signal power is around 20 dBFS at the beginning of the iterations, and it increases by 11 dB and reaches approximately 31 dBFS at the end of the iterations. As clearly seen in Figure 3.2, the RIS performances at different distances for the same angle exhibit very similar patterns of enhancements on the received signal power. In fact, the increase in the received signal power is around 10 dB for the angles of 50° and 70° and approximately 12 dB for the angles of 130°. For the case of 110°, the RIS can only boost the received signal power by around 4 dB since the Rx SDR has higher received signal power because of the symmetrical position of the Rx with respect to the Tx.

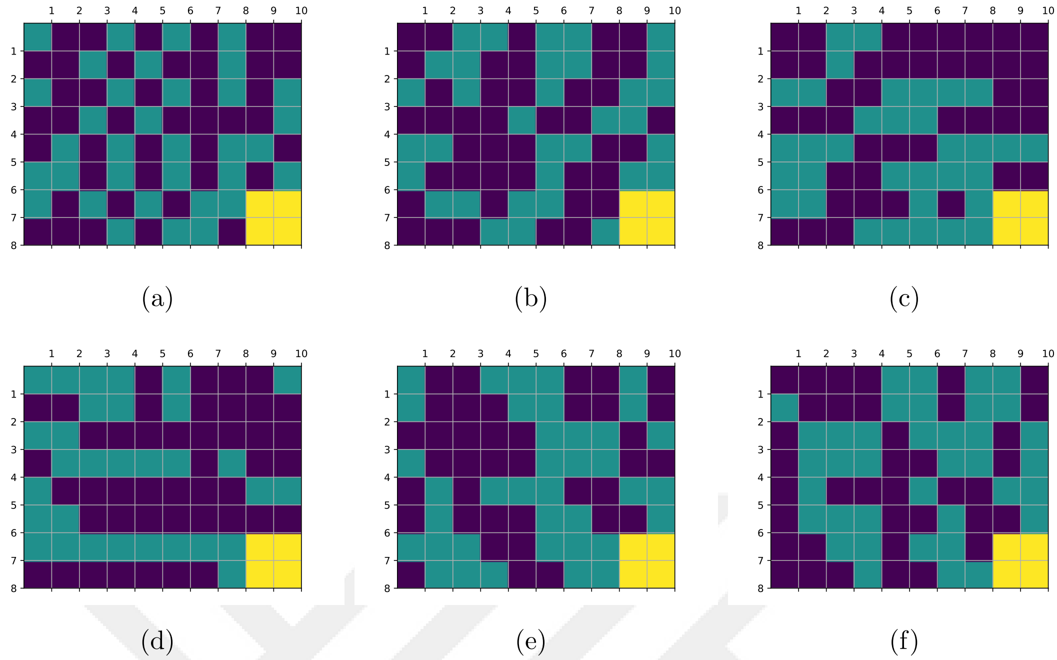

Figure 3.3: The codewords of the horizontal PIN diodes on/off configurations at the distance of 170 cm, and the angles of (a) 50°, (b) 70°, (c) 90°, (d) 110°, (e) 130°, and (f) 145°.

3.3.2 Codebook Implementation for Mobile Receiver

For mobile users, the RIS configuration has to be adjusted on the move in the coherence time of the channel between the RIS and Rx. The time spent during an iterative method like Algorithm 1 can exceed this, which the channel can be considered as stationary. Furthermore, for increasing data rates with reduced symbol duration, the time overhead of Algorithm 1 cannot be ignored. Thus, the implementation of a codebook, which contains the recorded RIS configurations for pre-determined points, can satisfy the time limitation of the channel by applying the saved RIS configurations based on the given locations of the terminals. Furthermore, the employment of a codebook for the RIS configurations eliminates the dependency of the feedback channel between the Rx and RIS, which is utilized to select the RIS configuration. Namely, the codebook-based approach can be employed by only requiring the geometric positions or the departure/arrival angles of the terminals. With this consideration, a codebook containing codewords of the RIS configurations for all

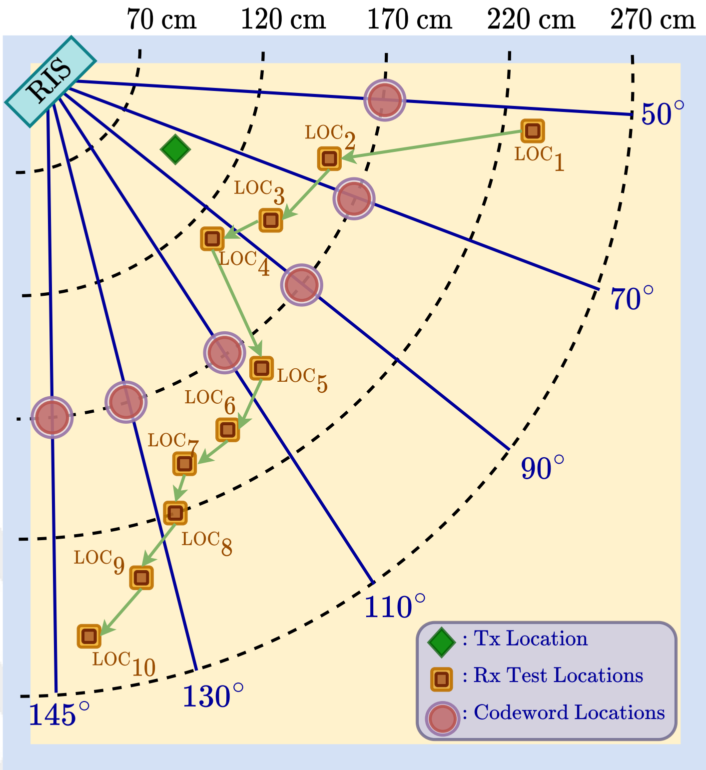

Figure 3.4: Top view of the considered RIS-assisted transmission scenario under the varying locations of the user.

the grid angles at 170 cm is generated using Algorithm 1 to be used afterward. The formed codewords of the horizontal PIN diodes on/off configurations are given in Figure 3.3. In the given configuration instances in Figure 3.3, the purple color represents the no-phase-shift mode of the RIS while the green color indicates the 180°-phase-shift mode and the yellow part corresponds to the RIS controller, which has no reflecting elements.

The Rx SDR's antenna is moved along the test points in the interior regions of the grids, and Figure 3.4 illustrates its path along the hallway. In Figure 3.4, pink circles represent the points where RIS configurations that maximize their received power are recorded to generate the codebook, while brown squares denote the locations of points where the mobile Rx moves.

During the movement of the Rx SDR's antenna, the codewords corresponding to the closest reference points are utilized to improve the performance of the Rx. The

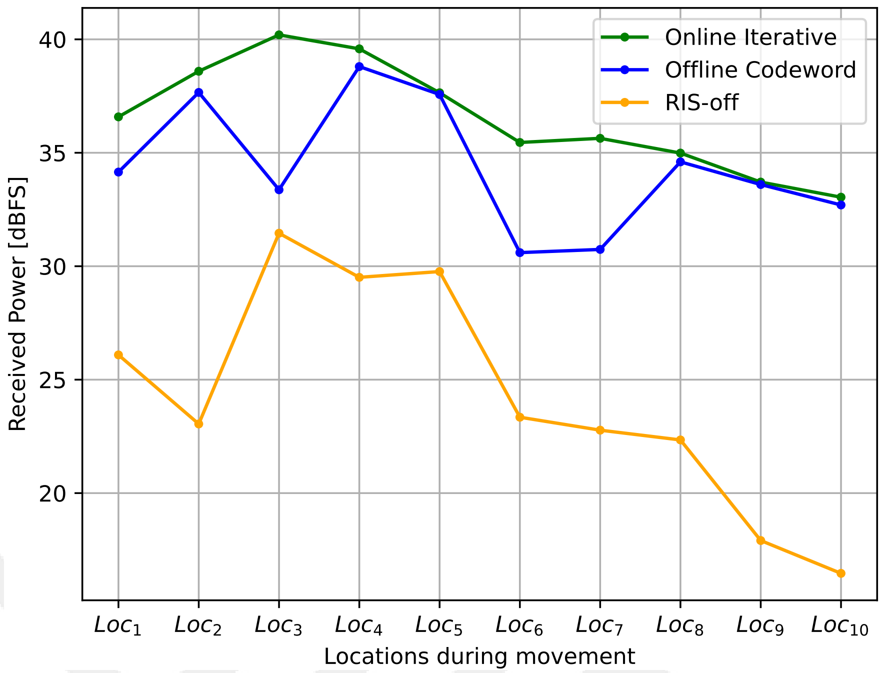

Figure 3.5: The comparison of received signal power during the Rx movement.

received signal powers are measured and compared for the three cases where: (i) the RIS is in no-phase-shift mode, (ii) the offline codeword of the stored codebook of the closest point is applied to the RIS, and (iii) the configuration of the online iterative method, which is derived via Algorithm 1 on the test point, is set to the RIS. Figure 3.5 shows the variation of the received signal powers of the mobile Rx through the test points for these three cases.

It can be observed from Figure 3.5 that the RIS configured with the codewords tends to keep the received signal powers above 30 dBFS even when the Rx moves further distances. Moreover, the performance of the codebook for locations where its angles are close to the angles of the saved codewords is observed to be very close to the results of online iterative configurations. Hence, using the offline codebook approach, the RIS can achieve comparable performance, which is approximately 3 dB lower than the real-time iterative method, without going through repeated iterations of Algorithm 1. Accordingly, this approach can fulfill the time constraint of the channel with an aid of a direction-finding algorithm since switching a codeword from another in the RIS takes approximately 1 ms [13].

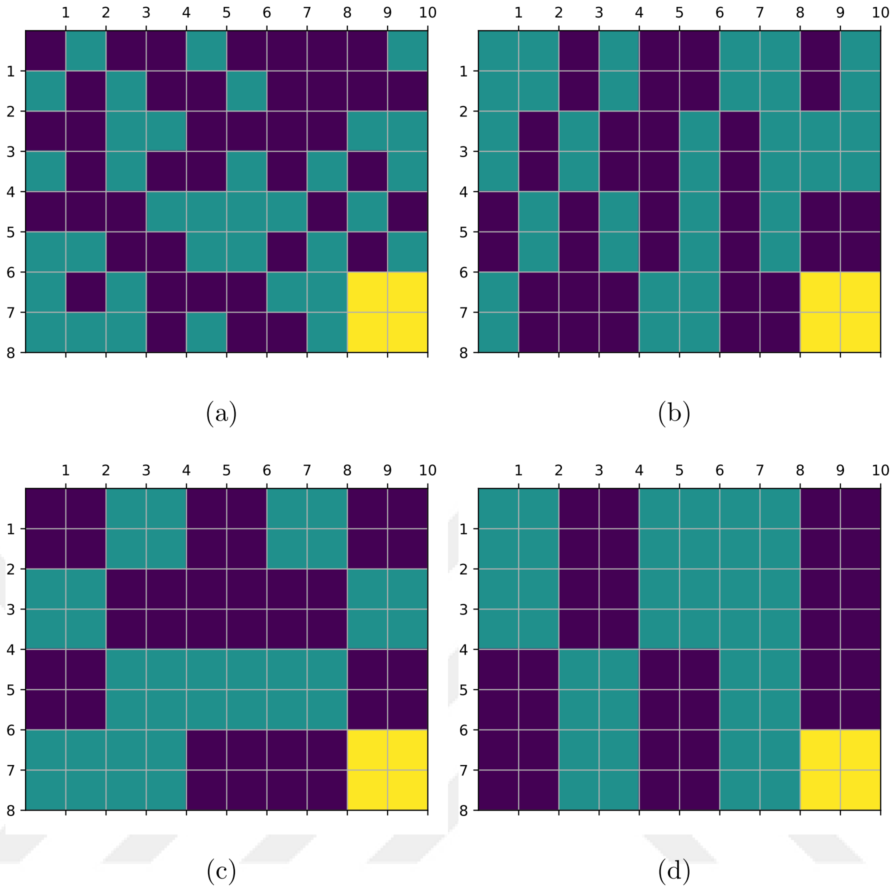

Figure 3.6: Examples the RIS configurations of (a) one-by-one, (b) two-by-two, (c) four-by-four, and (d) eight-by-eight grouping.

3.3.3 Effect of Grouping the RIS Elements

The number of RIS elements directly affects the training time required to determine optimal RIS configurations to steer the beam toward the Rx. The increasing number of RIS elements will also increase the reconfiguration overhead of the RIS. Therefore, one of the useful strategies for finding optimum RIS configuration is the sub-grouping of the RIS elements in the phase adjustment process. Another objective of grouping the RIS elements is to reduce the amount of time spent during the training process to generate the configuration that focuses the beam toward the Rx SDR. Figure 3.6 shows an example of the sub-grouped RIS configurations (only for one polarization of the RIS) with groups of two, four, and eight elements. The instances demonstrate how the grouping is applied.

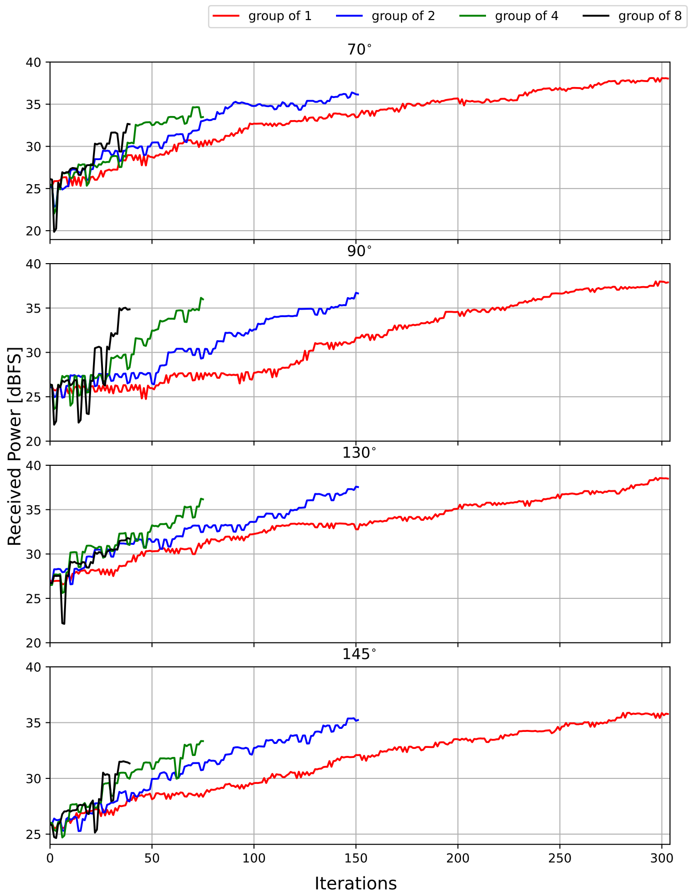

Figure 3.7: The received signal power during the iterations of Algorithm 1 for the grouping approach.

The received signal powers for the Rx angles of 70°, 90°, 130°, and 145° through the iterations of Algorithm 1, which are obtained from grouped elements, are shown in Figure 3.7. The given plots demonstrate the impact of grouping with two, four, and eight elements with respect to the increasing iteration. Figure 3.7 illustrates that the groups of two and four elements mostly perform close to the one-by-one adjustment case. For instance, even at 90°, the group of eight elements increases the received signal power by around 3 dB less than the single-element iterations. For most of the angles, the groups of two and four elements accomplish very close received signal power, within a few dB, in comparison to the one-by-one case. Thus, employing the grouping approach would significantly reduce the time and effort required to optimize the RIS configurations.

Chapter 4

RIS-ASSISTED PHYSICAL LAYER SECURITY

In this chapter, the characterization of RIS is demonstrated based on practical measurements for providing physical layer security (PLS), where the transmitter (Alice), the intended user (Bob), and the eavesdropper (Eve) are employed in an indoor environment. The theoretical framework of the PLS boosted by the RIS has been revealed in the literature, yet the measurement-based validation of the proposed architecture where RIS is situated to maximize the secrecy capacity of the wireless communication system is still an insufficient stage. At this stage, it is a challenging and open task to validate the RIS's ability to provide secure wireless communication in a practical measurement scenario by adjusting the RIS's phase shifts in a way that the difference between the received signal power of Bob and Eve is increased so that the secrecy capacity is maximized.

As utilizing the RIS in the task of PLS, the two main objectives of this chapter are (i) to derive the mathematical expression of the secrecy capacity of RIS-aided wireless communication system in terms of the received signal powers of Bob and Eve and (ii) to demonstrate the RIS's capability of handling PLS problem by increasing the secrecy capacity of the system via a measurement-based characterization.

4.1 System Model

As demonstrated in Figure 4.1, a basic secure wireless communication system where the RIS is utilized to maximize the secrecy capacity by increasing the difference between the received signal powers of Bob (intended user) and Eve (eavesdropper) in which Alice (transmitter) sends the over-the-air signal. In the considered system model, Alice transmits the signal to Bob through the RIS, and Eve tries to eavesdrop on the transmitted signal. The primary purpose of the RIS is to maximize

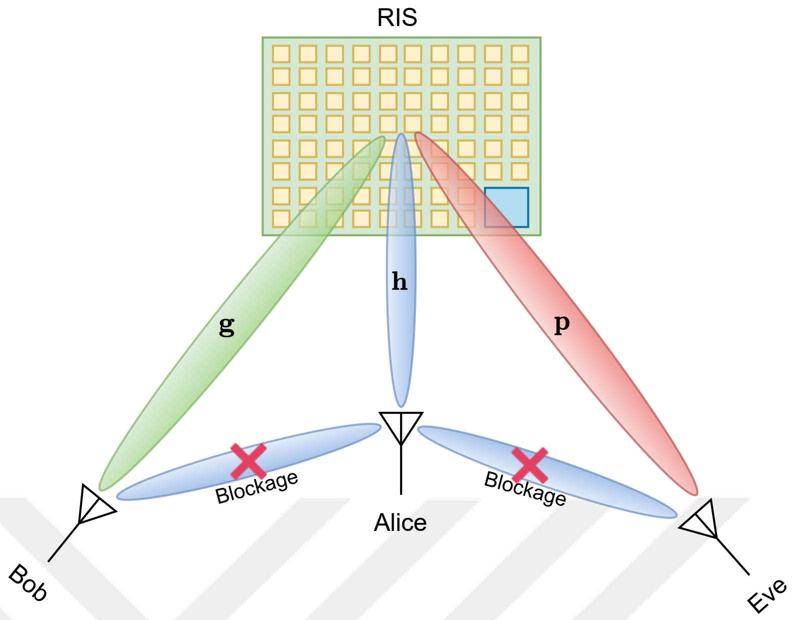

Figure 4.1: The considered RIS-assisted secure wireless communication system.

the secrecy capacity by boosting the received signal power of Bob while suppressing Eve's received signal power. The considered RIS in the system model and measurement setup consists of a uniform planar array structure containing $N = N_x \times N_y$ reflecting elements, which are illustrated as yellow squares in Figure 4.1. And the blue square indicates the RIS's controller, which handles the adjustment of each reflecting element's phase response via PIN diodes as 0° and 180° phase shifts. The terminals are placed in a way that the beams of their horn antenna don't intersect with each other so that the direct links between the terminals are not available, and the transmission and reception of the signal occur only through the RIS's reflected signals.

The channel from Alice to the RIS is represented as $\mathbf{h} \in \mathbb{C}^N$ while the channels from the RIS to Bob and Eve are depicted as $\mathbf{g} \in \mathbb{C}^N$ and $\mathbf{p} \in \mathbb{C}^N$, respectively. The direct links from Alice to Bob and Eve are neglected due to the fact that horn antennas, whose half beamwidth is 40°, are employed in the terminals to transmit and receive signals so that the direct link is out of the antennas' beamwidth. Accordingly, with $x[k]$ being the complex baseband signal transmitted by Alice, the received signal at Bob, $r_b[k]$, and the eavesdropped signal at Eve, $r_e[k]$, can be written as follows

$$\begin{aligned} r_b[k] &= \left(\mathbf{g}^H \mathbf{\Theta} \mathbf{h}\right) x[k] + n_b[k], \\ r_e[k] &= \left(\mathbf{p}^H \mathbf{\Theta} \mathbf{h}\right) x[k] + n_e[k], \end{aligned} \tag{4.1}$$

where $n_b[k] \sim \mathcal{N}_{\mathbb{C}}\left(0, \sigma_{n_b}^2\right)$ and $n_e[k] \sim \mathcal{N}_{\mathbb{C}}\left(0, \sigma_{n_e}^2\right)$ represent the noise component at Bob and Eve, respectively, and $\mathbf{\Theta}$ depicts the configuration matrix of the RIS. The configuration matrix is designated as $\operatorname{diag}\left\{\alpha_1 e^{j\phi_1}, \cdots, \alpha_N e^{j\phi_N}\right\}$, whose diagonal entries indicate the states of the RIS elements. Since the RIS elements are passive and binary-phased in the considered RIS prototype, α_n is constant, and ϕ_n takes values of only $0°$ and $180°$.

4.2 Secrecy Capacity

This section provides an analysis of the secrecy capacity of the proposed RIS-assisted wireless communication system in terms of the received signal powers of Bob and Eve based on the system model described in Section 4.1. After deriving the expression for the secrecy capacity, an iterative algorithm whose objective is to maximize the secrecy capacity by adjusting the phase shifts of each RIS element is presented.

The secrecy capacity of the wireless communication system where Alice transmits the signal to Bob while Eve attempts to eavesdrop on the sent signal can be expressed using the signal-to-noise ratio (SNR) of Bob, γ_b, and Eve, γ_e, as follows

$$\begin{aligned} C_s &= \max\Big(\log_2\left(1+\gamma_b\right) - \log_2\left(1+\gamma_e\right), 0\Big) \\ &= \max\left(\log_2\left(1+\frac{S_b}{N_b}\right) - \log_2\left(1+\frac{S_e}{N_e}\right), 0\right) \\ &= \max\left(\log_2\left(\frac{S_b+N_b}{N_b}\right) - \log_2\left(\frac{S_e+N_e}{N_e}\right), 0\right) \\ &= \max\Big(\log_2(S_b+N_b) - \log_2(N_b) - \log_2(S_e+N_e) + \log_2(N_e), 0\Big), \end{aligned} \tag{4.2}$$

where S_b and S_e represent the signal powers of Bob and Eve, respectively, while N_b and N_e depict the noise powers of Bob and Eve, respectively. The secrecy capacity can be expressed by using the received signal and noise powers as

$$C_s = \max\left(\log_2(P_b) - \log_2(P_e) + \log_2(N_e) - \log_2(N_b), 0\right), \tag{4.3}$$

where the received signal powers P_b and P_e at Bob and Eve. Assuming that $n_b[k]$ and $n_e[k]$ are independent white Gaussian noise components, P_b and P_e in (4.3) can be derived using the received signals $r_b[k]$ and $r_e[k]$ given in (4.1) as following expressions

$$\begin{aligned} P_b &= \left|\mathbf{g}^H \mathbf{\Theta} \mathbf{h}\right|^2 P_a + N_b, \\ P_e &= \left|\mathbf{p}^H \mathbf{\Theta} \mathbf{h}\right|^2 P_a + N_e, \end{aligned} \tag{4.4}$$

where P_a is the transmitted power from Alice.

The optimum phase shift configuration matrix $\mathbf{\Theta}^*$ that maximizes the secrecy capacity derived in (4.3) through substituting the received signal power expressions in (4.4) is determined as the following expression:

$$\begin{aligned} \mathbf{\Theta}^* = \arg\max_{\phi_n, \forall n} \Bigg(\max \Bigg(&\log_2 \left(\left|\mathbf{g}^H \mathbf{\Theta} \mathbf{h}\right|^2 P_a + N_b \right) - \log_2 \left(\left|\mathbf{p}^H \mathbf{\Theta} \mathbf{h}\right|^2 P_a + N_e \right) \\ &+ \log_2(N_e) - \log_2(N_b), 0 \Bigg) \Bigg) \\ \text{s.t. } & \phi_n \in \{0^\circ, 180^\circ\}, \quad \forall n. \end{aligned} \tag{4.5}$$

Solving the optimization problem given in (4.5) is quite a challenging and complicated task since the optimization problem is non-convex and the elements of $\mathbf{\Theta}^*$ can take only binary values of 0° and 180° in the considered RIS-aided wireless communication system.

In addition, the measurements of the received signal powers can be directly used as in (4.3) to calculate C_s in order to avoid going through the channel estimation procedure for practical scenarios. Therefore, the optimum phase shift configuration matrix, which directs the beam toward Bob and, at the same time, blocks the reflected beam for Eve, is determined utilizing the received signal powers of Bob and Eve. A straightforward iterative algorithm, inspired from [14], is utilized to find the RIS configurations to be used in a PLS application since all the possible RIS configurations of 4^{76} are infeasible to be performed through an exhaustive search in a practical scenario. A vector named *States* containing the phase shift configurations of the RIS is initialized with all 0° as a first step. Then, the four possible states of the first element in *StepList*, which consists of a shuffled list of element

Algorithm 2 Iterative algorithm for configuring RIS elements

Input: P_b, P_e, N, and S

Output: *States*

initialize *States* of RIS elements with $0°$ phase shift
$C_{s,max} \leftarrow -\infty$
StepList $\leftarrow$ shuffle $[1, N]$
for $i \in$ *StepList* **do**
    for $j = 1$ to S **do**
        configure state j to ith element
        measure P_b and P_e
        calculate C_s assuming that $N_b = N_e$
        if $(C_s > C_{s,max})$ **then**
            update ith element of *States* with state j
            $C_{s,max} \leftarrow C_s$
        end if
    end for
end for
return *States*

order, are applied, and the corresponding element of the RIS is kept in the state that maximizes the secrecy capacity computed by the received powers of Bob and Eve. After deciding on the first element's state in the list, the same procedure is individually performed for each of the remaining elements. The summary of the iterative phase shift method is provided in Algorithm 2, where P_b and P_e denote measured received signal powers of Bob and Eve, respectively, and the secrecy capacity calculated through (4.3) and the obtained maximum secrecy capacity are represented as C_s and $C_{s,max}$, respectively. Also, S represents the number of RIS states for one element. In order to analytically analyze the behavior of the RIS in a PLS measurement scenario, Algorithm 2 runs for approximately 100 times with randomly shuffled *stepList* of the RIS elements order in the algorithm.

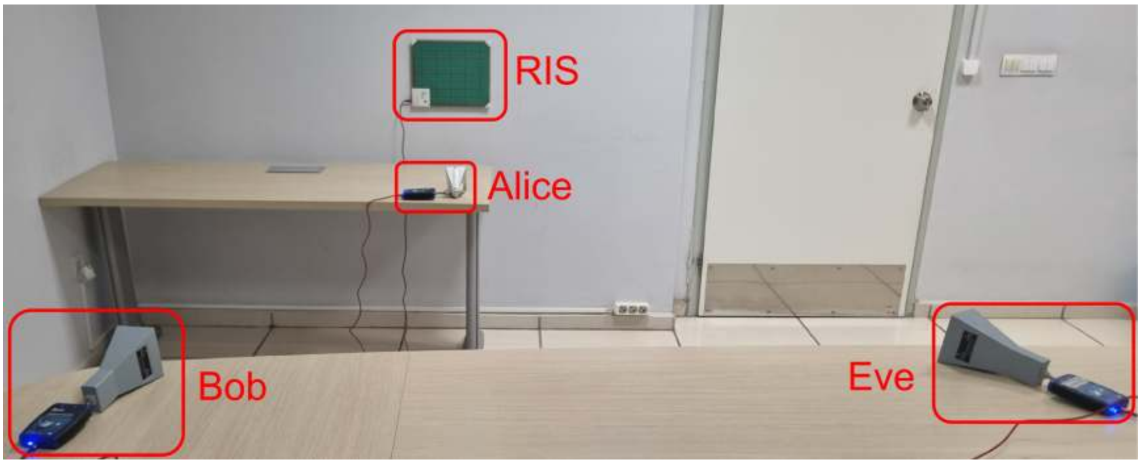

Figure 4.2: The measurement setup of the RIS-assisted wireless communication system.

4.3 Practical Secrecy Measurements

The measurement setup of the RIS-aided wireless communication system, which is assembled in an indoor office environment by utilizing ADALM-PLUTO SDR modules to transmit and receive over-the-air signals, is illustrated in Figure 4.2. Alice is placed in front of the RIS, which is attached to the wall, while Bob and Eve are located further away from the RIS, as shown in Figure 4.2. The Greenerwave RIS prototype [29] is utilized to direct the beam from Alice to Bob while eliminating the beam against Eve by software-controlled phase shifts. The RIS comprises a uniform planar array form with 8×10 reflecting elements, but the left bottom corner of the 2×2 area is allocated for the controller, resulting in the total number of 76 elements. The phase shift of each reflecting element can be independently controlled as $0°$ or $180°$ with two PIN diodes corresponding to the horizontal and vertical polarizations, ending up with four distinct states.

During the measurement campaign, a Python script controls the RIS by a Boolean array of 152 elements corresponding to PIN diodes where 0 and 1 represent $0°$ and $180°$ phase shifts, respectively. The sampling rate of the terminal SDRs is set to 1 MHz while the buffer size of SDRs for both Bob and Eve, the number of time samples to compute the average received signal power, is selected

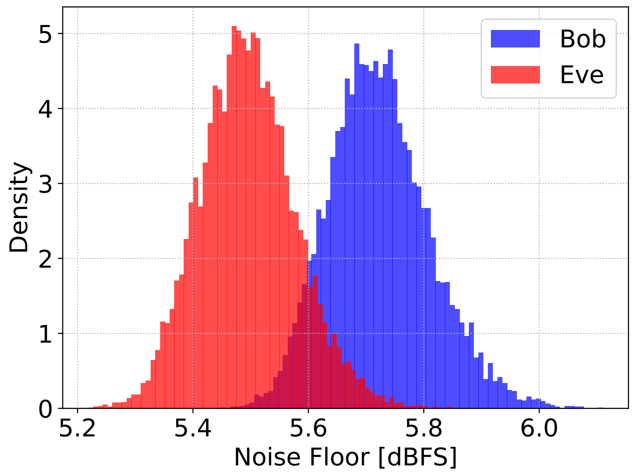

Figure 4.3: Noise Floor Densities of Bob and Eve.

as 10000. Alice transmits a single-tone sinusoidal signal of 100 kHz at the center frequency of 5.2 GHz using a horn antenna facing the RIS, and the reflected signal from the RIS reaches the horn antennas of Bob and Eve. Each SDR captures the incoming signal at 5.2 GHz and converts it to the complex baseband. The obtained complex baseband samples are depicted by integers in the range of $(-2047, 2048]$ since the SDR has a 12-bit analog to digital converter. Thus, the average power of the sampled received signal $r[k]$ can be calculated in the decibels relative to full scale (dBFS) as

$$P_{dBFS} = 10 \log_{10} \left(\frac{1}{K} \sum_{k=1}^{K} |r[k]|^2 \right), \tag{4.6}$$

where K stands for the total number of samples. The measured average received signal powers of Bob and Eve are substituted as P_b and P_e in Algorithm 2 to determine the phase shift configurations of the RIS that maximize the secrecy capacity by steering the beam toward Bob while absorbing the reflected beam to Eve.

Figure 4.3 illustrates the noise floor densities of Bob and Eve that are obtained from 11400 measurements in order to endorse the assumption made in Algorithm 2 that the noise floor of Bob and Eve is quite close to each other. The difference between the mean values of noise densities is approximately 0.228 dB, which can be ignored. Therefore, the secrecy capacity defined in (4.3) can be calculated by neglecting the difference in noise powers of Bob and Eve.

Table 4.1: The locations (x, y, z) of Alice, Bob, and Eve in meter.

	Alice	Bob	Eve
Loc1	(0.00, -0.35, 0.80)	(-0.54, -0.35, 2.70)	(1.20, -0.35, 2.60)
Loc2	(0.00, -0.35, 0.80)	(1.20, -0.35, 2.60)	(-0.54, -0.35, 2.70)
Loc3	(-0.40, -0.35, 0.46)	(-0.10, -0.35, 2.60)	(0.80, -0.35, 3.80)

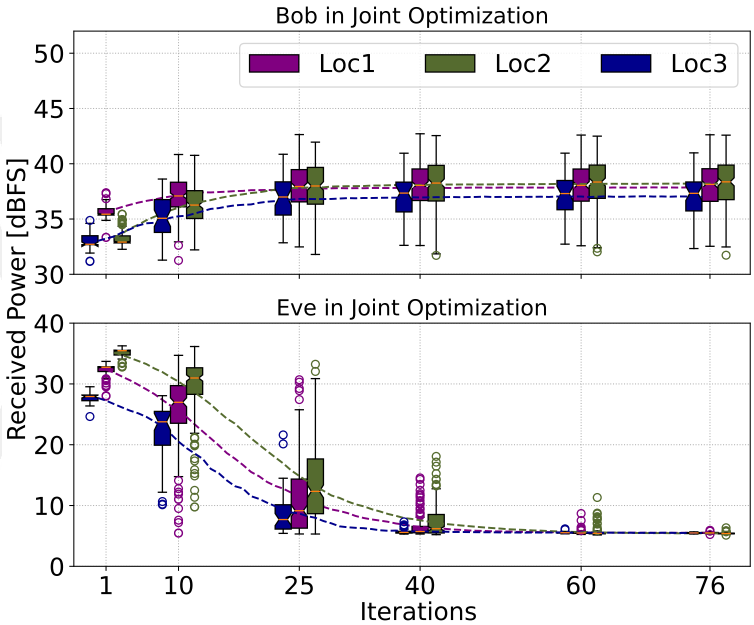

Figure 4.4: Measurement results of the received powers when the objective is to maximize the secrecy capacity.

The impact of the RIS on the received signal powers of Bob and Eve using Algorithm 2 is demonstrated by performing a set of measurement experiments at three different locations given in Table 4.1, where the RIS is placed at the origin. For each location, approximately 100 measurements are conducted aiming to maximize the secrecy capacity, where the order of elements in *StepList* is randomly chosen for each measurement. The received signal powers for Bob and Eve through the iterations of Algorithm 2 are illustrated in Figure 4.4 for three locations, where the mean values for each iteration are shown as dashed lines. In addition, the minimum, first quantile, third quantile, and maximum values of the received signal powers are

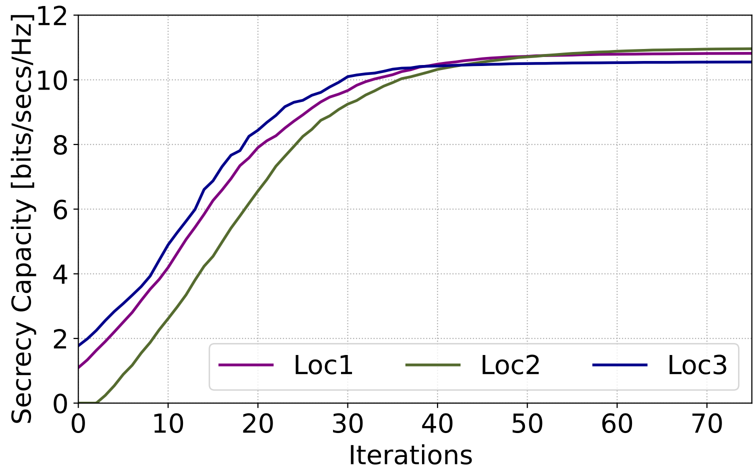

Figure 4.5: The average secrecy capacities for the measurement experiments.

depicted in consecutive order as the edges of the boxplots, while the median and the outliers are shown as the orange line and the circles in the plot. The results indicate that the received power of Bob increases by approximately 5 dB on average while the received power of Eve falls down to the noise floor. Note that the behaviors of the measurement results in Figure 4.4 demonstrate that Bob's received signal powers improve mostly around the first iterations. At the same time, Eve's received signal powers saturate at the noise floor through the end of the iterations in the measurement since the sensitivity of the PLUTO SDR is not sufficient to receive the signals below 5 dBFS.

The corresponding secrecy capacity results of the RIS-aided PLS scenario are illustrated in Figure 4.5, where the secrecy capacity is calculated by (4.3) with the received signal powers of Bob and Eve, which are optimized through Algorithm 2. Figure 4.5 demonstrates the average secrecy capacities of approximately 100 measurements for each location in terms of the iterations of Algorithm 2. As can be observed from Figure 4.5 that the secrecy capacities are significantly increased up to 11 bps/Hz. The secrecy capacities for all locations increase rapidly until settling down around the iteration 40, which is quite similar to the received signal powers of Bob and Eve given in Figure 4.4. In fact, the tendency of the secrecy capacity lines is consistent with Figure 4.4.

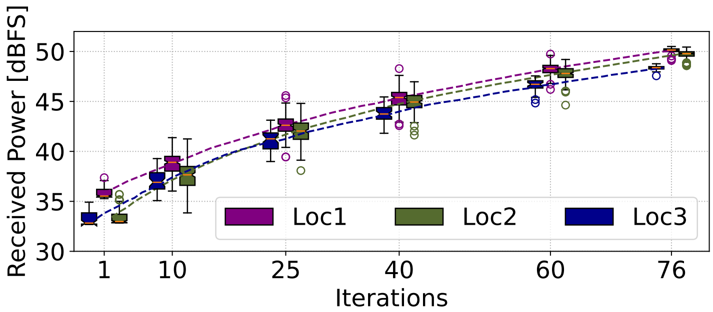

(a)

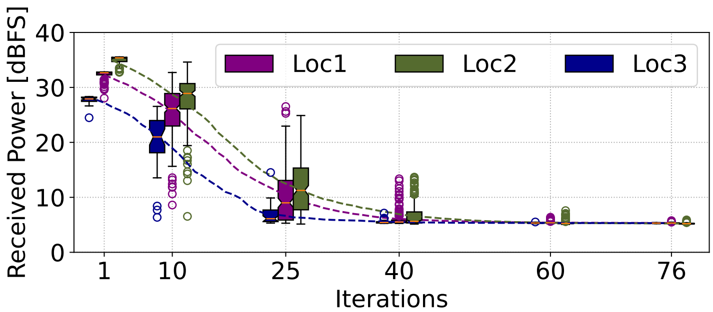

(b)

Figure 4.6: Measurement results of received power of (a) Bob when the objective is to maximize the received power, (b) Eve when the objective is to minimize the received power.

The individual optimizations for Bob to boost its received signal power and for Eve to block the reflected beam are separately considered in order to investigate the performance of the RIS in detail. The received signal power of Bob increases by 14 dB on average when the objective is set to maximize the received power of Bob only as demonstrated in Figure 4.6a while the received signal power of Eve falls down to the noise floor when the objective is set to minimize the received power of Eve only as shown in Figure 4.6b. It can be observed from Figure 4.6 that the iterative algorithm prioritizes to further decreasing Eve's received signal power to improve the secrecy capacity since there exist many regions with low signal powers in the reflected beam of the RIS.

Chapter 5

RIS-ENHANCED SPECTRUM SENSING

In this chapter, the RIS-empowered spectrum sensing system, in which the object detection approach by deep-learning (DL) methods is utilized to determine the signal's type and location on the frequency and time domain, is demonstrated via a measurement campaign. Incorporating the RIS into the spectrum sensing system will have a substantial impact on improving the quality of spectrum sensing methods since there exists a direct correlation between the received signal power and the performance of the spectrum sensing process.

In deploying the RIS into the spectrum sensing system, the two main goals of this chapter are (i) to train two state-of-art object detectors in order to utilize and compare their performance in the spectrum sensing problem and (ii) to exhibit the improvement of introducing the RIS into the spectrum sensing system by illustrating the performance increases of the detectors.

5.1 System Model

As represented in Figure 5.1, a basic spectrum sensing system where the RIS is employed to assist the secondary user (SU) in monitoring the parameters of the signal broadcasted by the primary transmitter (PT) to be conveyed toward the primary receiver (PR). The communication between the PT and the PR takes place through a line-of-sight (LoS) link, assuming that the reflected signal from the RIS to the PR can be neglected compared to the LoS signal. The communication between the PT and SU occurs through a direct link and the reflected signals from the RIS. The main objective of the RIS is to maximize the received signal power by the SU through the RIS.

The employed RIS in the system model and experiments is formed by $N =$

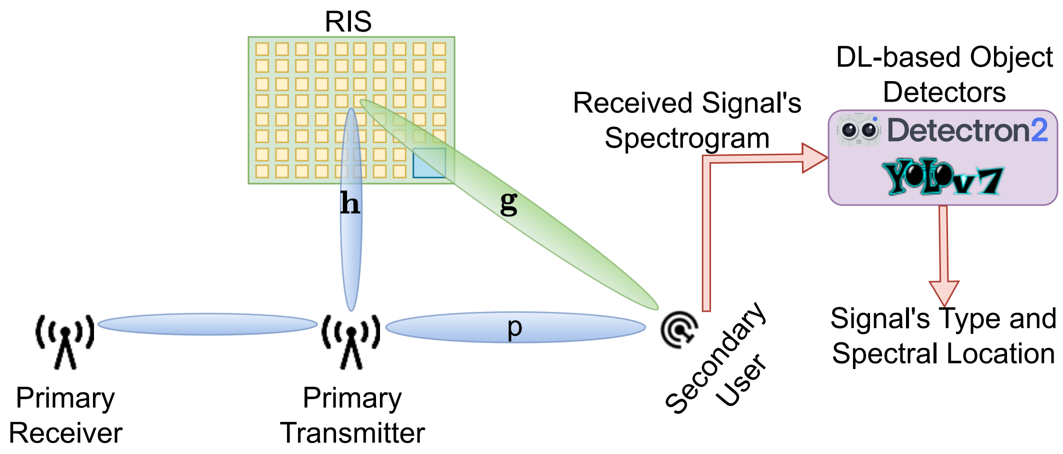

Figure 5.1: The RIS-empowered spectrum sensing system.

$N_x \times N_y$ reflecting elements in the structure of a uniform planar array, which are depicted as yellow squares in Figure 5.1. The controller represented by the blue square at the bottom right corner of the RIS is used to provide the dynamic phase adjustment for each reflecting element as 0° or 180° using PIN diodes.

The channel from the PT to the RIS is denoted as $\mathbf{h} \in \mathbb{C}^N$, the channel from the RIS to SU is represented as $\mathbf{g} \in \mathbb{C}^N$, and the channel between the PT and SU is denoted as $p \in \mathbb{C}$. During the spectrum sensing process, the SU can receive either the complex baseband signal, $x[k]$, transmitted by the PT or the empty spectrum. Accordingly, the $\mathcal{H}_0$ hypothesis indicates the PT is in idle mode, whereas the $\mathcal{H}_1$ hypothesis denotes the PT is in transmit mode. Hence, the received signal at the SU, $r[k]$, under the hypotheses of $\mathcal{H}_0$ and $\mathcal{H}_1$ can be expressed as follows

$$\begin{aligned} &\mathcal{H}_0 : r[k] = n[k], \\ &\mathcal{H}_1 : r[k] = \left(\mathbf{g}^H \boldsymbol{\Theta} \mathbf{h} + p\right) x[k] + n[k], \end{aligned} \tag{5.1}$$

where $n[k] \sim \mathcal{N}_{\mathbb{C}}\left(0, \sigma_n^2\right)$ indicates the noise component at the SU, and $\boldsymbol{\Theta}$ represents the phase shift configuration matrix of the RIS's reflecting elements. The configuration matrix is described as diag $\left\{\alpha_1 e^{j\phi_1}, \cdots, \alpha_N e^{j\phi_N}\right\}$, whose diagonal entries depict the phase shift states of the RIS elements. The value of α_n is constant, and ϕ_n takes values of only 0° and 180° because the reflecting elements of the RIS are passive and binary-phased in the considered RIS.

5.2 DL-based Spectrum Sensing

Spectrum sensing, which is a core approach for cognitive radio networks, is an enabling technology that detects, localizes, and classifies signals in the frequency and time domain. Cognitive radio networks aim to maximize spectrum efficiency by dynamically managing the spectrum usage of the PT and SU with the help of spectrum sensing. Namely, the SU tracks the occupancy of the spectrum during the spectrum sensing process and can transmit a signal whenever the PT is not active in its operating frequencies.

Many traditional signal processing methods for spectrum sensing have been introduced in the literature, such as adaptive thresholding, energy detection, matched filtering, and cyclostationary feature extraction. However, these traditional algorithms experience certain weaknesses, such as poor performances at low received signal powers, requirements for prior signal information, and high complexity to operate in a real-time application. Nonetheless, the upcoming next-generation communication technologies have more tendency for applications of the Internet of Everything and massive machine-type communication that network elements have minimal signal processing ability and low transmit power. Therefore, DL-based solutions, which have proven their efficiency for many applications in wireless communication, can be implemented to overcome the deficiencies of the traditional approaches and to present a ready-to-use method in a real-time application with the assistance of state-of-art object detection approaches.

Since the detection performance of the spectrum sensing process heavily depends on how much the PT's signal power reaches the SU, the RIS plays a critical role in improving the success of the spectrum sensing procedure by increasing the received signal power of the SU. Hence, introducing the RIS into the spectrum sensing system will provide certain improvements in the spectrum sensing performance.

5.2.1 State-of-art Object Detectors: Detectron2 and YOLOv7

Object detection, whose objective is to localize and classify objects in a target image, is one of the active areas in computer vision. This area has an array of applications, from the classification and location of enemy threads in synthetic aperture radar images to the detection of cancer cells in magnetic resonance imaging images. The objective of this chapter is to detect, classify, and localize the PT signals on images that illustrate the frequency and time domain recordings of the signals. Two of the most popular object detectors in DL-based approaches are Detectron2 [30], which Facebook AI Research (FAIR) developed as an open-source library that presents state-of-the-art detection and segmentation methods, and ”You Only Look Once” (YOLO)v7 [31], which is a revised version of YOLO [32].

Detectron2 is the FAIR’s library, which provides state-of-art open-source object detection and segmentation algorithms. Detectron2 is presented in a flexible structure in order to facilitate the rapid deployment and assessment of forthcoming research in the computer vision area. In fact, Detectron2 includes many employments for a variety of DL-based object detection and segmentation methods, such as Faster R-CNN, Mask R-CNN, TensorMask, PointRend, RetinaNet, DensePose, etc.

YOLOv7 is an upgraded version of YOLO that allows the target image to be handled as a network input and directly returns the bounding box probabilities and locations of the detected objects. YOLO is a neural network consisting of a single end-to-end structure, which divides each target image into grids whose purpose is to detect objects when their centers intersect a grid cell. It has been reported in [31] that YOLOv7 outperforms many known object detectors in terms of the inference speed and accuracy thanks to its re-parameterization of the model network and dynamic label assignment.

5.2.2 Network Parameters of the Detectors

The transfer learning approach, in which the pre-trained weights are utilized to train the new model, is implemented in order to reduce the training effort. In fact, the pre-trained weights are trained with the Common Objects in Context (COCO) dataset for both detector networks to be used without training all the network layers from the beginning. Detectron2[1] and YOLOv7[2] detector networks whose open-source codes are shared publicly, are correspondingly updated to the spectrum sensing problem. The training and testing of the detectors are completed with a server containing a central processor unit of Intel Xeon Platinum, a graphics processing unit of Nvidia Tesla V100S 32GB, and a random access memory of 64GB.

The Detectron2's detector is implemented with the mask R-CNN architecture initiated with the pre-trained model of *mask_rcnn_X_101_32x8d_FPN_3x*[1]. Additionally, the detector is trained with a learning rate of 0.0025, an image per batch of 16, a batch size per image of 512, and 4000 iterations with every 20 iteration corresponding to an epoch.

The YOLOv7's detector is started to be trained with the pre-trained model of *yolov7*[2]. In addition, the batch and epoch sizes of the detector are chosen as 64 and 200, respectively.

5.2.3 Signals of Interest, Dataset Representation and Generation

In the investigated spectrum sensing system, the PT can transmit three sets of signals, such as fourth-generation long-term evolution (4G LTE) signal, fifth-generation new radio (5G NR) signal, and both 4G LTE and 5G NR signals at the same time. These signal transmission scenarios are simulated using MATLAB's LTE and 5G NR Toolboxes, which include built-in functions compliant with the standards, example codes, validation, and simulation of the LTE and 5G communication systems. The signals of the three transmission scenarios of the PT are simulated by utilizing MATLAB's toolboxes.

The simulated signals are represented as spectrograms by taking a sampling rate of 60 MHz and a signal duration of 40 ms. Also, the spectrograms, which are illustrated as an JPG file with 256×256 pixels whose examples are shown in Figure 5.2, are handled through a Hanning window with an overlapping ratio of 10% and an FFT size of 4096. The rows and columns in Figure 5.2 indicate the frequency and

---

[1] Available at: https://github.com/facebookresearch/detectron2

[2] Available at: https://github.com/WongKinYiu/yolov7

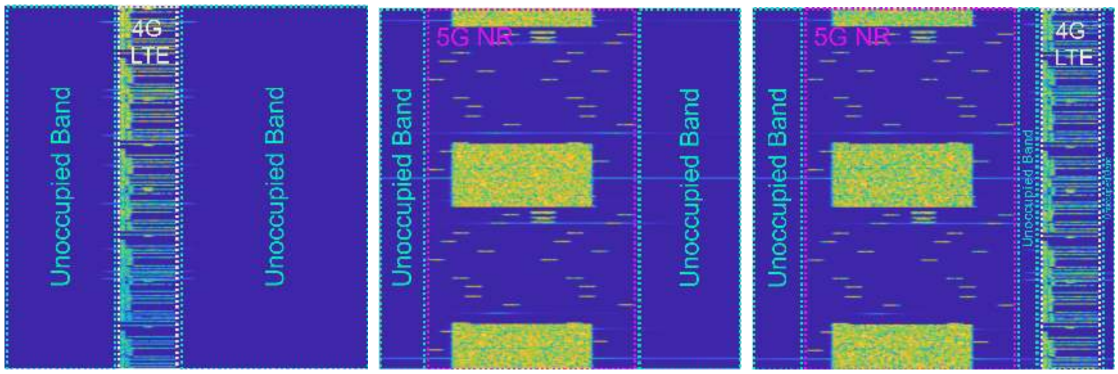

(a) (b) (c)

Figure 5.2: The spectrograms of the transmitted signals of (a) 4G LTE, (b) 5G NR, and (c) both 4G LTE and 5G NR.

time domains of the signals, respectively. Additionally, the colormap depicts the signal strength, with blue representing a low signal power and yellow representing a high signal power.

A synthesized dataset consisting of spectrograms of the PT's transmission signals is generated through MATLAB to train the object detectors. The parameters for the 4G LTE signals are chosen as frequency division duplexing and the bandwidth of $\{5, 10, 15, 20\}$ MHz, whereas the parameters for the 5G NR signals are selected as the subcarrier spacing of $\{15, 30\}$ kHz and the bandwidth of $\{10, 15, 20, 25, 30, 40, 50\}$ MHz. In addition, the target signal-to-noise ratio (SNR) values of $\{0, 20, 50\}$ dB and the target Doppler values of $\{0, 10, 500\}$ Hz are set for the channel conditions. For each signal transmission scenario, 900 different signals for training and 300 signals for testing are generated with MATLAB's simulated channels. Therefore, there are 2700 spectrogram images to be fed to the detectors to train and 900 spectrogram images to test the trained detectors for all three scenarios. Note that these signals are generated using the example code in Mathworks website [33]. Instead of the SNR values of $\{-10, 0, 50\}$ dB, we utilize $\{0, 20, 50\}$ dB since the RIS increases the received signal power at the SU by focusing the reflected signals towards the SU. This ensures that the detectors are trained using a more suitable dataset.

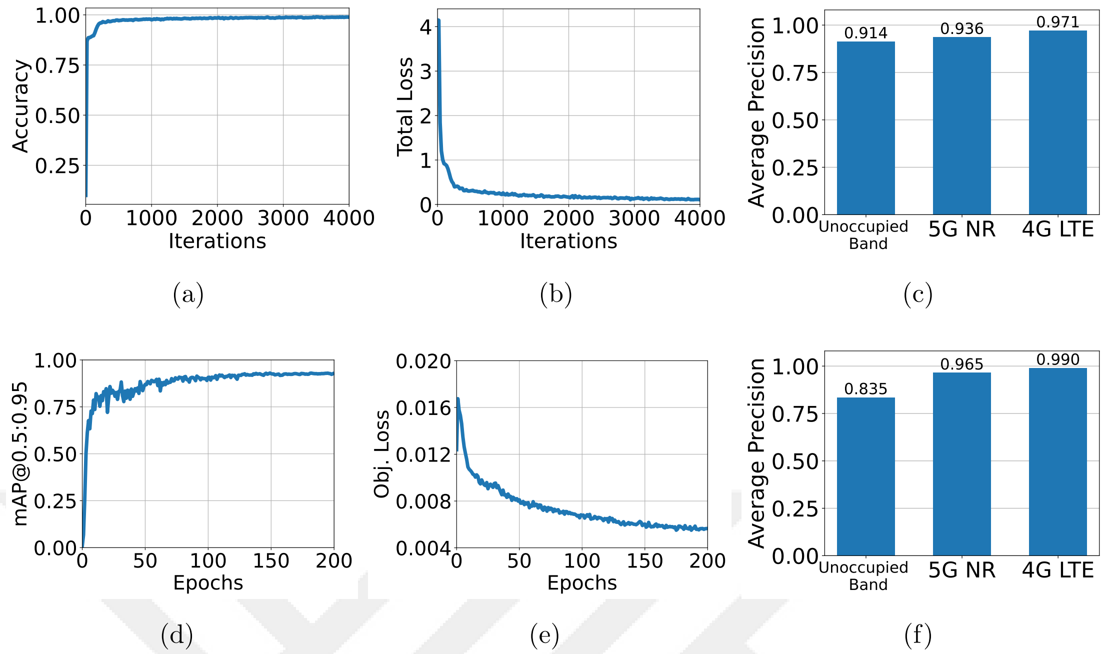

Figure 5.3: Detectron2's (a) accuracy, (b) total loss, and (c) average precision with the test dataset; YOLOv7's (d) mAP@0.5:0.95, (e) objectness loss, and (f) average precision with the test dataset.

5.2.4 Results of the Detectors under Simulation Test Dataset

The training dataset of 2700 spectrograms is fed to Detectron2 and YOLOv7 models to train their weights. These detectors are utilized to identify the 4G LTE, 5G NR, and unoccupied bands on spectrogram images. Figures 5.3a and 5.3b illustrate the accuracy of Detectron2 and its total loss with respect to the number of training iterations, respectively. As the number of iterations increases, the accuracy rapidly approaches towards unity while the total loss decreases towards zero. The total loss is the weighted sum of the classification, localization, and mask losses. The average precision (AP) values of the trained Detectron2 model, which are obtained by the test dataset including 900 spectrogram images, are shown in Figure 5.3c. The AP values of the unoccupied band, 5G NR, and 4G LTE are higher than 0.91, and the highest AP of 0.971 is achieved for 4G LTE. The SU can transmit its signals when there are no 5G NR and 4G LTE signals of the PT. In addition, the SU can transmit its signals using only unoccupied regions of the spectrum when there are

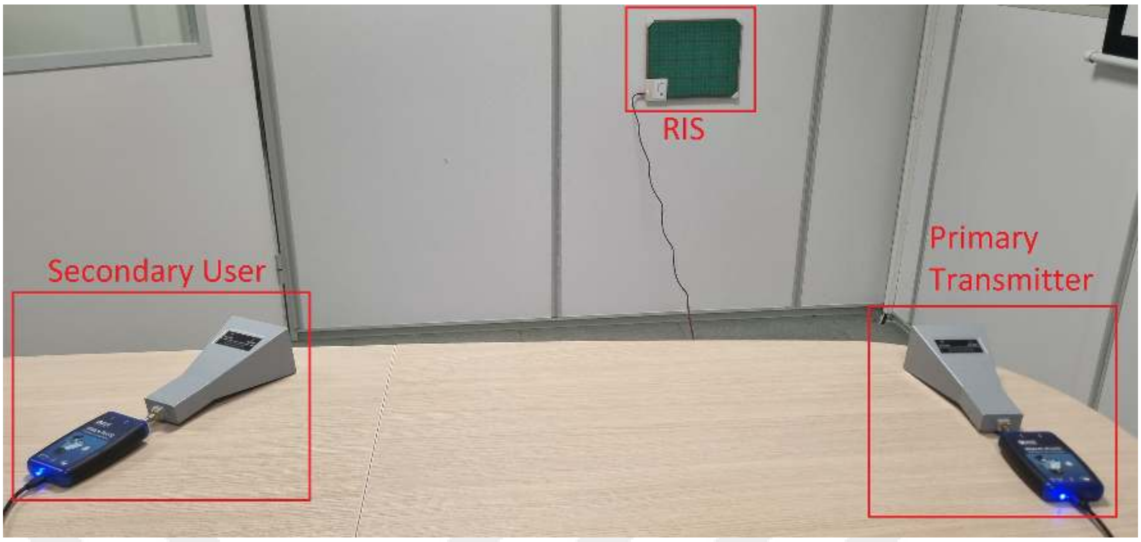

Figure 5.4: The measurement setup of the RIS-enhanced spectrum sensing system.

5G NR and 4G LTE signals. For the YOLOv7 detector's training process, the mean AP (mAP), which is calculated at the intersection over union (IoU) from 0.50 to 0.95 with the step size of 0.05 (mAP@0.5:0.95), is shown in Figure 5.3d. Note that the IoU measures the overlapping of predicted signal boundaries with the real signal boundaries. The objectness loss through the epochs is shown in Figure 5.3e. As the number of training epochs increases, the model precision improves while the objectness loss decreases. The AP values of the trained YOLOv7 model, which are obtained by the test dataset including 900 spectrogram images, are shown in Figure 5.3f. The results show that YOLOv7 can detect 4G LTE and 5G NR signals more accurately, while Detectron2 can identify unoccupied bands better. Note that these trained models will be utilized in practical measurements, including the RIS, in the following section. The test results indicate that the models are successfully trained. However, it is suggested to use the results of practical measurements to compare the performance of the models.

5.3 Performance Analysis of the Detectors in Practical Measurement

The measurement setup of the RIS-enhanced spectrum sensing system is illustrated in Figure 5.4. The experiments are conducted with ADALM-PLUTO SDR modules

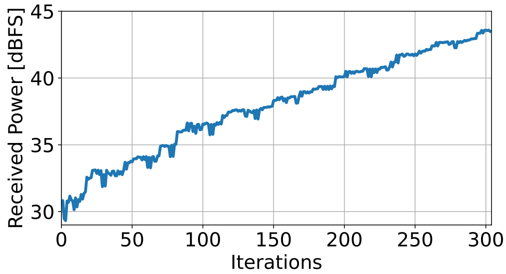

Figure 5.5: The received signal power during the iterations of Algorithm 1.

to realize the over-the-air transmission and reception by the PT and SU, respectively. The PT and SU are located to ensure that their horn antenna beams remain non-intersecting, resulting in the reception of the reflected signal from the PT only through the RIS-assisted path. The Greenerwave RIS prototype [29] operating at 5.2 GHz is located on the wall to boost the power of the received signals by the SU by adjusting the phase shifts of the reflecting elements. The RIS is formed in the structure of a uniform planar array with 8×10 reflecting elements, but its left bottom corner of 2×2 region is designated for its controller, ending up with a total of 76 reflecting elements. Each element's phase shift can be individually adjusted by two PIN diodes, which correspond to the horizontal and vertical polarization, as $0°$ and $180°$, resulting in four different states.

Throughout the measurement process, 300 generated in-phase and quadrature data by MATLAB containing signals for the three transmission scenarios are transmitted by the PT's SDR module. Then, the SU's SDR module records the spectrograms of the received signals to be passed through the spectrum sensing procedure in order to localize and classify the signals via the detectors of Detectron2 and YOLOv7. The measurements are taken for two scenarios, where (I) the RIS is in off mode, specifying that the reflecting element phase shifts are set to $0°$, and (ii) the RIS operates in an optimized state, configuring the reflecting elements to maximize the received signal power at the SU.

Figure 5.5 illustrates the increase in the received signal power in terms of the iterations of Algorithm 1 given in Chapter 3. As can be observed from Figure 5.5 that the received signal power of the SU is boosted by approximately 13 dB. Thus,

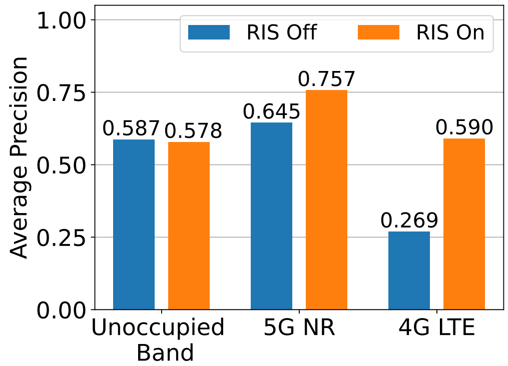

(a)

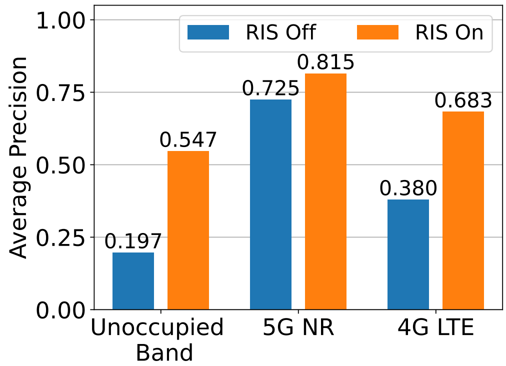

(b)

Figure 5.6: The AP results using the measurement dataset when the RIS is off and on for (a) Detectron2 and (b) YOLOv7.

the signals monitored by the SU become much more apparent in the spectrogram representation with the increase in the signal power.

Figure 5.6 demonstrates the AP results of the detectors with the collected 300 spectrograms from over-the-air by the SU's SDR for the two cases corresponding to the RIS being off and on. For the Detectron2, the optimized RIS configuration has the most significant impact on the 4G LTE signal by remarkably enhancing the AP from 0.269 to 0.590. Additionally, the AP of the 5G NR signal is increased from 0.645 to 0.757, while a slight reduction is observed for the unoccupied band. For the YOLOv7, the AP of the 4G LTE signal is raised from 0.380 to 0.683, the 5G NR signal's AP is boosted by 0.09, and the highest improvement of 0.350 is obtained for the unoccupied band portion of the signal. The performance of both detectors is improved for the signals of interest (i.e., 4G LTE and 5G NR) by introducing the RIS into the spectrum sensing system. Overall, YOLOv7 performs better than Detectron2 except for detecting the unoccupied band for both cases of RIS's operation modes. Therefore, utilizing YOLOv7 in the spectrum sensing process for determining the activities of the PT is more reasonable, as it demonstrates superior detection performance for the signals of interest. On the other hand, employing Detectron2 in the spectrum sensing system would be proper for the SU to determine the unused bands in the spectrum and utilize them.

Chapter 6

RIS-ASSISTED 5G MMWAVE COMMUNICATION

In this chapter, the validation of the millimeter wave (mmWave) RIS prototype's performance with a vector network analyzer (VNA) in an anechoic chamber and the evaluation of the RIS with the fifth-generation (5G) waveform operating at the mmWave frequency band in a data center are performed. A preliminary step prior to the deployment of the mmWave RIS into a real-world environment is the validation of its performance under ideal conditions, such as in an anechoic chamber. In fact, link management in a data center is one of the possible playgrounds of RIS employment since rack cabinets cause severe blockage for the wireless communication system in the room. The investigation of the mmWave RIS performance with 5G waveform in a data center plays a crucial role in future applications of the RIS.

In exploring the performance of the mmWave RIS prototype, the two main targets of this chapter are (i) to verify the mmWave RIS's performance in a perfect environment like an anechoic chamber and (ii) to examine the signal power improvement of 5G waveform running in the mmWave frequency band, which is introduced by the RIS deployed in a data center.

6.1 MmWave RIS Prototype and Measurement Setups

The physical structure of the considered mmWave RIS, which is shown in Figure 6.1, is a uniform planar array with 40×40 reflecting elements with a half-wavelength spacing. Each configurable reflecting element on the RIS has a binary phase shift adjustment with $0°$ and $180°$ which is controlled by two PIN diodes corresponding to horizontal and vertical polarization. The RIS operates at frequencies ranging from 26 GHz to 31 GHz within an instantaneous bandwidth of 3 GHz with a less than 3 dB reflection loss. The scan range of the RIS's reflected beam in both azimuth

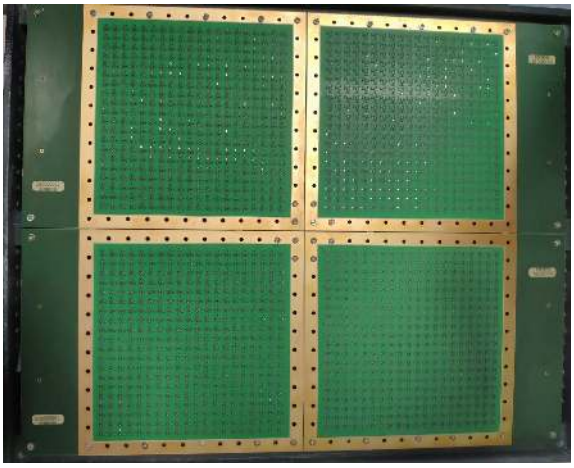

Figure 6.1: The front of the MmWave RIS prototype.

Table 6.1: The mmWave RIS specifications.

Number of reflecting elements	1600
Reflecting element scaping	half-wavelength
Number of phase adjustments	binary ($0°$ and $180°$)
Polarization	dual (horizontal and vertical)
Operating frequency range	$[26-31]$ GHz with instantaneous 3 GHz
Reflection loss within bandwidth	< 3 dB
Beam scan range (elevation, azimuth)	$\pm 60°$
Directivity	30 dBi
Beam switch speed (remote/saved)	1 kHz / 100 kHz

and elevation is $\pm 60°$ with 30 dBi directivity. An FPGA control card independently manages the switching of the total number of 3200 PIN diodes to adjust the phase shift of each reflecting element in both polarization. The speed of the switching process is in the order of kHz when the RIS is controlled with a computer via a USB port, and the rate is 100 kHz if saved configurations in the local memory of the FPGA card are applied. The power consumption of the RIS ranges from 3 W to 16 W, with an average of 6 W. The mmWave RIS prototype [29] considered in the measurements whose aperture size is 20 cm $\times$ 20 cm as shown in Figure 6.1 and its specifications are summarized in Table 6.1 [14].

Figure 6.2: The measurement setup constructed to validate the performance of the mmWave RIS in a anechoic chamber.

Two distinct measurement campaigns are investigated in the course of this chapter's experiments of RIS-assisted wireless communication, whose objective is to increase the received signal power with the help of the reflected beams from the RIS. In the first experiment, a VNA is utilized to transmit an over-the-air signal toward the RIS and receive the reflected signal from the RIS in an anechoic chamber in order to observe the performance of the mmWave RIS. In the second experiment, the mmWave RIS is utilized to improve the signal coverage of the 5G waveform by increasing the received signal power in a data center where a 5G base station working at mmWave frequency ranges is deployed.

6.2 Validation of the RIS with VNA in the Anechoic Chamber

The measurement setup of RIS-assisted wireless communication, which is established to validate the performance of the mmWave RIS, is illustrated in Figure 6.2. VNA is set to measure the scattering parameter of S_{21}, which corresponds to the forward voltage gain and is obtained by taking the linear ratio of the output reflected power waves to the input incident power waves. In fact, the S_{21} parameter can be used to

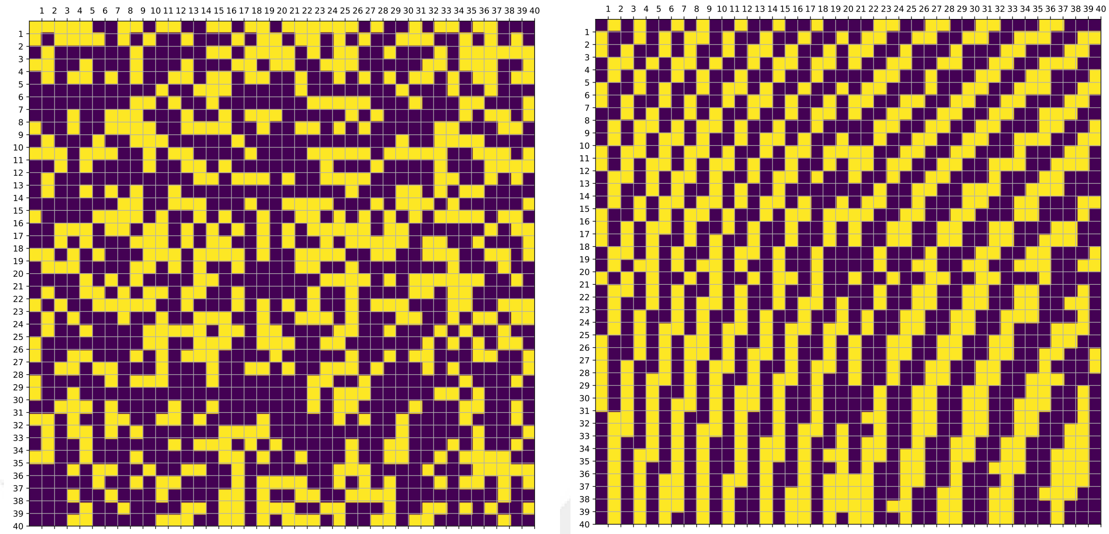

(a) (b)

Figure 6.3: The RIS elements of PIN diodes on/off configurations in the given positions of antennas and RIS at the frequency range of [27.5 − 29.5] GHz for (a) horizontal and (b) vertical polarization.

monitor the delivered signal power of the VNA's receiver port from its transmitter port. In the anechoic chamber, the mmWave RIS is placed in front of the VNA's transmitter and receiver ports on which horn antennas with vertical polarization are connected. The mmWave RIS is attached to a computer via its USB port in order to be controlled its reflecting elements' phase shift configurations. Simultaneously, the same computer is connected to the VNA via an Ethernet port in order to access the VNA's real-time S_{21} measurements, which serve as feedback to the RIS in the optimization process. The VNA is set to measure the S_{21} parameters in the frequency range from 27.5 GHz to 29.5 GHz with 401 points and delivers its real-time readings to the computer.

The iterative optimization method of Algorithm 1 proposed in Chapter 3 is modified to maximize the magnitude of the S_{21} parameter. In the algorithm, the received signal power, P_r, is substituted with the S_{21} feedback from the VNA, and the optimization parameter is chosen as S_{21}. Figure 6.3 illustrates the vertical polarization configuration of the reflection elements optimized via Algorithm 1, which

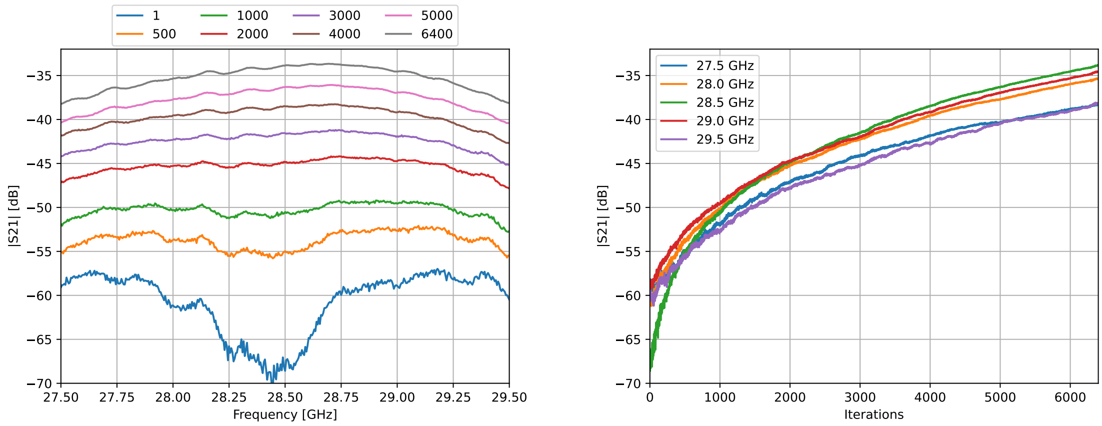

(a) (b)

Figure 6.4: The S_{21} parameters (a) with respect to the frequencies for various iterations of Algorithm 1, and (b) with respect to the iterations for various frequencies.

runs through its iterations in order to maximize the S_{21} parameter for the frequencies between 27.5 and 29.5 GHz. In the obtained configuration instance given in Figure 6.3, the blue color indicates that the corresponding PIN diode is off, which means that the reflecting element's phase shift is $0°$ while the yellow color represents that the corresponding PIN diode is on meaning that the reflecting element's phase shift is $180°$. As can be observed from Figure 6.3a that the RIS configuration corresponding to the horizontal polarization appears to be randomly configured, whereas Figure 6.3b displays that the RIS configuration associated with the vertical polarization seems to have a pattern since the horn antennas used for the transmission and reception of the signal have vertical polarization and the wireless communication is realized in the vertical polarization.

Figure 6.4 shows the obtained improvement from the RIS at the frequencies from 27.5 GHz to 29.5 GHz by implementing Algorithm 1 to increase the S_{21} parameters read from the VNA in the anechoic chamber. The S_{21} parameter through the frequencies $[27.5-29.5]$ GHz for the iterations $\{1, 500, 1000, 2000, 3000, 4000, 5000, 6400\}$ of Algorithm 1 is plotted in Figure 6.4a. Meanwhile, Figure 6.4b illustrates the S_{21} parameter with respect to the iterations of Algorithm 1 for the frequencies of $\{27.5, 28.0, 28.5, 29.0, 29.5\}$ GHz. The performances of the RIS throughout the fre-

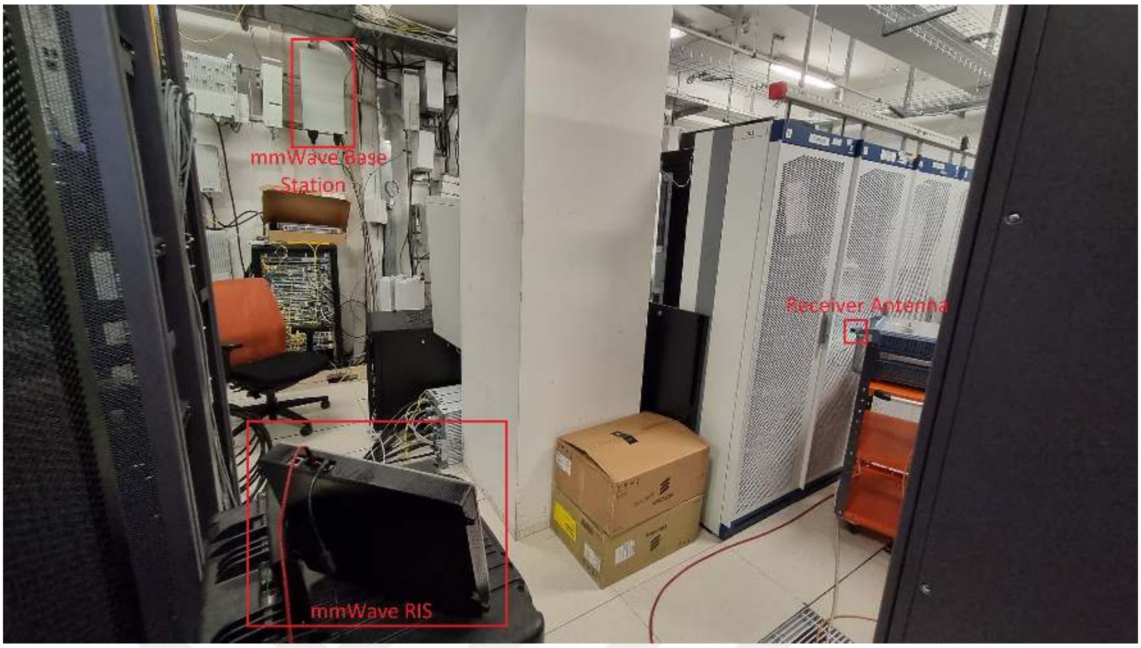

Figure 6.5: The measurement setup assembled to evaluate the performance of the mmWave RIS in a data center.

quencies exhibit similar patterns of increase in the S_{21} parameter as around 25 dB improvement except for the frequencies between [28.25 – 28.75] GHz, where the RIS provides approximately 35 dB gain. Therefore, the experiment accomplished in the anechoic chamber verifies the performance of the mmWave RIS at frequencies ranging from 27.5 GHz to 29.5 GHz.

6.3 Evaluation of the RIS with 5G Waveform in a Data Center

The experiment setup of the RIS-aided wireless communication system with a base station transmitting 5G waveform at mmWave frequency band, which is constructed in order to analyze the performance of the mmWave RIS prototype in a data center, is shown in Figure 6.5. The data center located in the testing building of Turkcell, which is one of the mobile phone operators of Turkiye, has rack cabinets containing computer servers that require extremely high throughput between each other. In fact, realizing the transmission of this throughput between the computers via a wireless communication system is one of the use cases of the future generation of wireless networks. Moreover, the RIS can enhance the signal coverage of the wireless

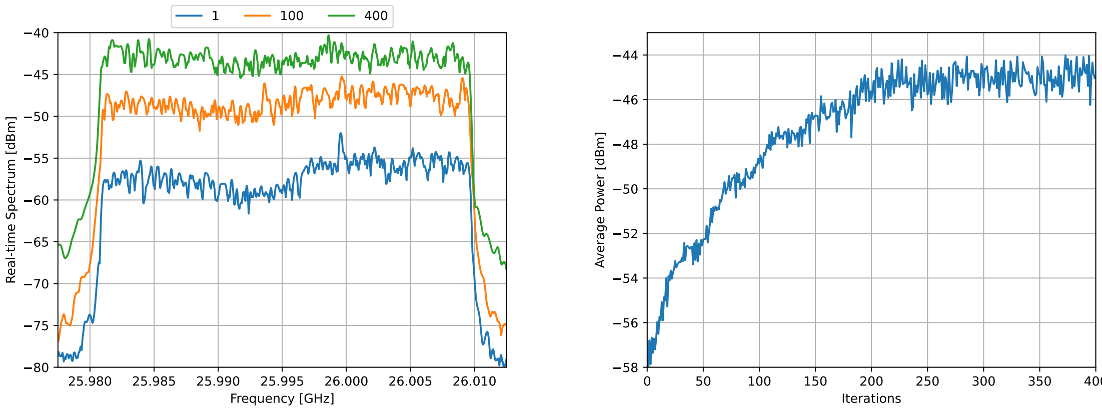

(a) (b)

Figure 6.6: For the first placement, (a) the real-time spectrum of 5G SSB signal for the Algorithm 1 iterations, and (b) the average power during the iterations.

data transmission between the computers in the data center and accommodate a virtual line-of-sight connection between them.

In the experiment, the 5G base station transmits the Synchronization Signal Block (SSB) of the 5G waveform with 30 MHz bandwidth at the center frequency of 25.995 GHz, which is received by the horn antenna attached to a spectrum analyzer. A computer is connected to the spectrum analyzer via an Ethernet port to read the spectrum analyzer's real-time measurements, which provide feedback in the optimization process to the RIS, which is connected to the same computer via its USB port in order to be controlled its reflecting elements' phase shift configurations. The real-time readings of the spectrum are exploited to measure the average signal power to be used in the iterative method of Algorithm 1 given in Chapter 3. Additionally, the concept of grouping the reflecting elements, which is introduced in Subsection 3.3.3, is implemented in the measurement to reduce the amount of time and energy spent over the optimization process since the number of reflecting elements is much more for the mmWave RIS.

The measurement campaign to evaluate the performance of the mmWave RIS in the data center for the 5G waveform's SSB signal is carried out for two different locations of the receiver and the RIS. Figures 6.6 and 6.7 illustrate the results of

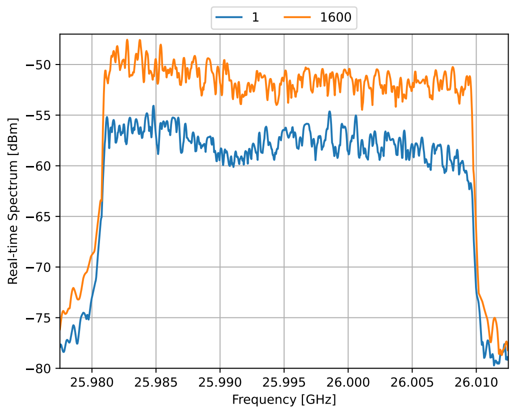

(a)

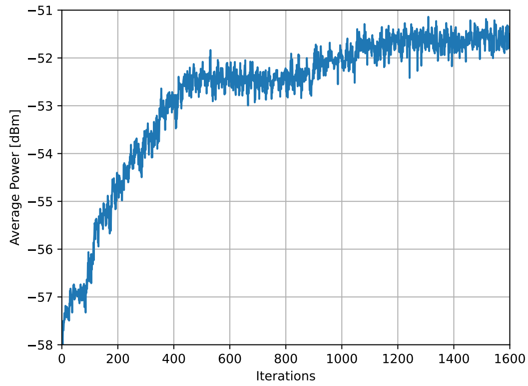

(b)

Figure 6.7: For the second placement, (a) the real-time spectrum of 5G SSB signal for the Algorithm 1 iterations, and (b) the average power during the iterations.

the measurements for the RIS positions of 3 m and 8 m from the base station, respectively. The former placement is shown in Figure 6.2, where the receiver is positioned 2 m away from the RIS, blocking the line-of-sight connection between the base station and the receiver. At the latter positioning, the receiver is placed 3 m away from the RIS with similar angles as the previous one.

Figures 6.6a and 6.6b, where the RIS's elements are grouped with 16 elements as a 4×4 structure, illustrate the real-time spectrum for the Algorithm 1 iterations of $\{1, 100, 400\}$ and the average power throughout the iterations for the first placement, respectively. As can be observed from Figures 6.6, the average power of the SSB signal increases around 13 dB with the help of the RIS. Moreover, Figures 6.7a and 6.7b, where the RIS's elements are grouped with 4 elements as a 2×2 structure, depict the real-time spectrum for the Algorithm 1 iterations of $\{1, 1600\}$ and the average power over the iterations for the second placement, respectively. For this positioning, the RIS provides approximately 5 dB average power improvement since the second placement has a more channeling environment, where the RIS is positioned further away from the base station. Namely, the signal power that reached the RIS from the base station, which will be reflected by the RIS's element toward the receiver, is much less than the first measurement.

Chapter 7

CONCLUSION

In this thesis, the practical deployments of the RIS have been presented for various use-case scenarios, which are potential applications in future-generation networks. Firstly, a real-world RIS has been employed in a system operating at 5.2 GHz to manipulate the over-the-air signals in an indoor environment in order to enhance the signal coverage by improving the received signal power. With the help of the proposed iterative algorithm, the fully passive RIS provides a significant increase in the received signal power for different angles and distances from the RIS. In order to reduce the RIS configuration overhead, a phase shift codebook for the geometric positions of the Tx and Rx has also been designed to be implemented at the nearest test points. For the considered measurement setup, the saved codewords achieve similar performance in comparison to the online iterative results, and the RIS with the codewords is able to provide reliable transmission throughout the movement of the Rx. The proposed grouping strategy for the RIS elements is considered to reduce the training time needed to determine the RIS configurations. By means of the efficient grouping strategy, the training time is significantly decreased by losing only a few dBs.

Secondly, the considered RIS prototype has been implemented in a wireless communication system, where an RIS is utilized to provide physical layer security (PLS). This task is accomplished by manipulating the wireless propagation environment by adjusting the reflecting elements' phase shift in a way that the reflected beams are steered toward Bob while suppressing the reflected beams reaching Eve. The measurement campaign for the constructed system model in an indoor environment for the PLS demonstrates that the secrecy capacity can be substantially increased with the aid of the RIS with the assumption of the availability of Eve's power measurements.

Thirdly, an RIS-enhanced spectrum sensing system, where the secondary user monitors the activities of the primary transmitter with deep-learning detectors, has been proposed. The state-of-art detectors of Detectron2 and YOLOv7, which are utilized to estimate the signal's parameters, such as signal type and location in the spectrum, are trained with the spectrograms of the synthesized signal dataset of 4G LTE and 5G NR. The trained detectors are tested for their performance in two practical measurement environments in which the RIS is in off mode and optimized to focus the reflected beam toward the secondary user. The results show that the RIS significantly improves the average precision of the detectors in the spectrum sensing task.

Finally, the performance validation of a mmWave RIS prototype has been achieved in an anechoic chamber by obtaining approximately 25 dB gain in S_{21} parameter for its operating frequencies. Then, the RIS's deployment scenario of the data center with the 5G mmWave signal is implemented to improve the received signal power. The measurements in the data center demonstrate that incorporating the mmWave RIS into the room of blockages caused by rack cabinets provides improvements in received signal power.

Overall, it is concluded that these measurement campaigns might be useful to more clearly understand the practical utilization aspects of RISs in challenging applications and environments. Future directions might include the implementation and demonstration of the novel use cases of the RISs deployed for the future generation of wireless communication networks and also the derivation of the theoretical models for these experiments to compare with the measurement results and reveal the differences.

BIBLIOGRAPHY

[1] K. Buchholz, "Where 5G technology has been deployed," https://www.statista.com/chart/23194/5g-networks-deployment-world-map/, 2022, [accessed July 30, 2022].

[2] E. Basar and I. Yildirim, "Reconfigurable intelligent surfaces for future wireless networks: A channel modeling perspective," *IEEE Wireless Commun.*, vol. 28, no. 3, pp. 108–114, Apr. 2021.

[3] I. Yildirim, A. Uyrus, and E. Basar, "Modeling and analysis of reconfigurable intelligent surfaces for indoor and outdoor applications in future wireless networks," *IEEE Trans. Commun.*, vol. 69, no. 2, pp. 1290–1301, Nov. 2021.

[4] Y. Liu, X. Liu, X. Mu, T. Hou, J. Xu, M. Di Renzo, and N. Al-Dhahir, "Reconfigurable intelligent surfaces: Principles and opportunities," *IEEE Commun. Surveys & Tuts.*, vol. 23, no. 3, pp. 1546–1577, May 2021.

[5] E. Basar, I. Yildirim, and F. Kilinc, "Indoor and outdoor physical channel modeling and efficient positioning for reconfigurable intelligent surfaces in mmWave bands," *IEEE Trans. Commun.*, vol. 69, no. 12, pp. 8600–8611, Sept. 2021.

[6] E. Basar, "Reconfigurable intelligent surface-based index modulation: A new beyond MIMO paradigm for 6G," *IEEE Trans. Commun.*, vol. 68, no. 5, pp. 3187–3196, Feb. 2020.

[7] I. Yildirim, A. Koc, E. Basar, and T. Le-Ngoc, "RIS-aided angular-based hybrid beamforming design in mmWave massive MIMO systems," in *GLOBECOM 2022-2022 IEEE Global Communications Conference.* IEEE, Dec. 2022, pp. 5267–5272.

[8] B. Gao, J. Li, Z. Yu, J. Sang, M. Zhou, J. Lan, W. Tang, X. Li, and S. Jin, "Propagation characteristics of RIS-assisted wireless channels in corridors: Measurements and analysis," in *IEEE/CIC International Conference on Communications in China (ICCC)*, 2022, pp. 550–554.

[9] X. Pei, H. Yin, L. Tan, L. Cao, Z. Li, K. Wang, K. Zhang, and E. Björnson, "RIS-aided wireless communications: Prototyping, adaptive beamforming, and indoor/outdoor field trials," *IEEE Transactions on Communications*, vol. 69, no. 12, pp. 8627–8640, Sept. 2021.

[10] Z. Wang, L. Tan, H. Yin, K. Wang, X. Pei, and D. Gesbert, "A received power model for reconfigurable intelligent surface and measurement-based validations," in *IEEE 22nd International Workshop on Signal Processing Advances in Wireless Communications (SPAWC)*, 2021, pp. 561–565.

[11] A. Araghi, M. Khalily, M. Safaei, A. Bagheri, V. Singh, F. Wang, and R. Tafazolli, "Reconfigurable intelligent surface (RIS) in the sub-6 GHz band: Design, implementation, and real-world demonstration," *IEEE Access*, vol. 10, pp. 2646–2655, Oct. 2022.

[12] J. Rains, A. Tukmanov, T. J. Cui, L. Zhang, Q. H. Abbasi, M. A. Imran *et al.*, "High-resolution programmable scattering for wireless coverage enhancement: An indoor field trial campaign," *arXiv preprint arXiv:2112.11194*, Dec. 2021.

[13] J.-B. Gros, V. Popov, M. A. Odit, V. Lenets, and G. Lerosey, "A reconfigurable intelligent surface at mmWave based on a binary phase tunable metasurface," *IEEE OJ-COMS*, vol. 2, pp. 1055–1064, May 2021.

[14] V. Popov, M. Odit, J.-B. Gros, V. Lenets, A. Kumagai, M. Fink, K. Enomoto, and G. Lerosey, "Experimental demonstration of a mmWave passive access point extender based on a binary reconfigurable intelligent surface," *Frontiers in Communications and Networks*, vol. 2, p. 733891, 2021.

[15] L. Dai, B. Wang, M. Wang, X. Yang, J. Tan, S. Bi, S. Xu, F. Yang, Z. Chen, M. Di Renzo *et al.*, "Reconfigurable intelligent surface-based wireless communications: Antenna design, prototyping, and experimental results," *IEEE Access*, vol. 8, pp. 45 913–45 923, Mar. 2020.

[16] R. Fara, P. Ratajczak, D.-T. Phan-Huy, A. Ourir, M. Di Renzo, and J. De Rosny, "A prototype of reconfigurable intelligent surface with continuous control of the reflection phase," *IEEE Wireless Commun.*, vol. 29, no. 1, pp. 70–77, Feb. 2022.

[17] H. Zhang, S. Zeng, B. Di, Y. Tan, M. Di Renzo, M. Debbah, Z. Han, H. V. Poor, and L. Song, "Intelligent omni-surfaces for full-dimensional wireless communications: Principles, technology, and implementation," *IEEE Commun. Mag.*, vol. 60, no. 2, pp. 39–45, Feb. 2022.

[18] L. Yang, J. Yang, W. Xie, M. O. Hasna, T. Tsiftsis, and M. D. Renzo, "Secrecy performance analysis of RIS-aided wireless communication systems," *IEEE Transactions on Vehicular Technology*, vol. 69, no. 10, pp. 12 296–12 300, 2020.

[19] G. Zhou, C. Pan, H. Ren, K. Wang, and Z. Peng, "Secure wireless communication in RIS-aided MISO system with hardware impairments," *IEEE Wireless Communications Letters*, vol. 10, no. 6, pp. 1309–1313, 2021.

[20] J. Zhang, H. Du, Q. Sun, B. Ai, and D. W. K. Ng, "Physical layer security enhancement with reconfigurable intelligent surface-aided networks," *IEEE Transactions on Information Forensics and Security*, vol. 16, pp. 3480–3495, 2021.

[21] W. Xu, J. Zhang, S. Cai, J. Wang, and Y. Wu, "RIS-assisted MIMO secure communications with Bob's statistical CSI and without Eve's CSI," *Digital Communications and Networks*, 2022. [Online]. Available: https://www.sciencedirect.com/science/article/pii/S2352864822001699

[22] A. U. Makarfi, R. Kharel, K. M. Rabie, O. Kaiwartya, X. Li, and D.-T. Do, “Reconfigurable intelligent surfaces based cognitive radio networks,” in *2021 IEEE Wireless Communications and Networking Conference Workshops (WCNCW)*. IEEE, 2021, pp. 1–6.

[23] W. Wu, Z. Wang, L. Yuan, F. Zhou, F. Lang, B. Wang, and Q. Wu, “IRS-enhanced energy detection for spectrum sensing in cognitive radio networks,” *IEEE Wireless Communications Letters*, vol. 10, no. 10, pp. 2254–2258, 2021.

[24] S. Lin, B. Zheng, F. Chen, and R. Zhang, “Intelligent reflecting surface-aided spectrum sensing for cognitive radio,” *IEEE Wireless Communications Letters*, vol. 11, no. 5, pp. 928–932, 2022.

[25] A. Nasser, H. A. H. Hassan, A. Mansour, K.-C. Yao, and L. Nuaymi, “Intelligent reflecting surfaces and spectrum sensing for cognitive radio networks,” *IEEE Transactions on Cognitive Communications and Networking*, vol. 8, no. 3, pp. 1497–1511, 2022.

[26] J. Ge, Y.-C. Liang, S. Li, and Z. Bai, “Ris-enhanced spectrum sensing: How many reflecting elements are required to achieve a detection probability close to 1?” *IEEE Transactions on Wireless Communications*, vol. 21, no. 10, pp. 8600–8615, 2022.

[27] W. Wu, Z. Wang, Y. Wu, F. Zhou, B. Wang, Q. Wu, and D. W. K. Ng, “Joint sensing and transmission optimization for IRS-assisted cognitive radio networks,” *IEEE Transactions on Wireless Communications*, 2023.

[28] E. T. S. Institute, “ETSI GR RIS 001: Reconfigurable intelligent surfaces (RIS); use cases, deployment scenarios and requirements,” https://www.etsi.org/committee/1966-ris, 2023, [accessed July 7, 2023].

[29] Greenerwave, “Greenerwave 2022, 35 rue du Sentier, 75002 Paris, France,” https://greenerwave.com/, 2022, [accessed July 28, 2022].

[30] Y. Wu, A. Kirillov, F. Massa, W.-Y. Lo, and R. Girshick, "Detectron2," https://github.com/facebookresearch/detectron2, 2019, [accessed June 1, 2023].

[31] C.-Y. Wang, A. Bochkovskiy, and H.-Y. M. Liao, "Yolov7: Trainable bag-of-freebies sets new state-of-the-art for real-time object detectors," in *Proceedings of the IEEE/CVF Conference on Computer Vision and Pattern Recognition*, 2023, pp. 7464–7475.

[32] J. Redmon, S. Divvala, R. Girshick, and A. Farhadi, "You only look once: Unified, real-time object detection," in *Proceedings of the IEEE conference on computer vision and pattern recognition*, 2016, pp. 779–788.

[33] Mathworks, "Spectrum sensing with deep learning to identify 5G and LTE signals," https://www.mathworks.com/help/comm/ug/spectrum-sensing-with-deep-learning-to-identify-5g-and-lte-signals.html, 2023.